SEMMELWEIS EGYETEM

DOKTORI ISKOLA

Ph.D. értekezések

3521.

ZÖLDI MIKLÓS

Neuromorfológia és sejtbiológia
című program

Programvezető: Dr. Alpár Alán, egyetemi tanár

Témavezető: Dr. Katona István, tudományos tanácsadó

Advanced STORM super-resolution techniques for astrocyte-specific molecular imaging

PhD thesis

Miklós Zöldi

János Szentágothai Doctoral School of Neurosciences

Semmelweis University





Supervisor: István Katona, DSc

Official reviewers: Zoltán Hegyi, PhD
István Adorján, PhD

Head of the Complex Examination Committee: Alán Alpár, DSc

Members of the Complex Examination Committee: Miklós Réthelyi, DSc
Katalin Schlett, PhD

Budapest
2026

Table of Contents

List of abbreviations 3
1. Introduction 5
1.1. Super-resolution imaging as a way to overcome the diffraction barrier 5
1.2. SMLM imaging in neuroscience research 8
1.3. A growing demand for imaging astrocytic proteins at the nanoscale level 13
1.4. Monoacylglycerol lipase, a promising enzyme at the crossroads of endocannabinoid and prostaglandin signaling 15
2. Objectives 18
3. Methods 19
3.1. Animals 19
3.2. *In utero* electroporation 20
3.3. Preparation and labeling of embryonic brain sections 20
3.4. Postnatal astrocyte labeling by electroporation (PALE) 21
3.5. DNA constructs 22
3.6. Preparation of hippocampal sections 22
3.7. Immunolabeling 23
3.8. RNAscope *in situ* hybridization 24
3.9. Confocal imaging 25
3.10. Single-color and dual-color STORM image acquisition 25
3.11. Correlated confocal and STORM imaging 26
3.12. STORM image analysis 27
3.13. Statistical analysis and figure preparation 29
4. Results 31
4.1. Electroporation as a sparse labeling method for subsequent super-resolution imaging 31
4.1.1. Examining the architecture of radial glial cells labeled by *in utero* electroporation 31
4.1.2. STORM imaging reveals the nanoscale morphology of hippocampal astrocytes labeled by postnatal electroporation 34

4.2. Dual-color STORM imaging of hippocampal astrocytes in brain tissue 38
4.2.1. Microscopic control measurements for dual-color STORM imaging 38
4.2.2. Molecular imaging in sub-diffraction-limit astrocytic processes 42
4.3. Examining the nanoscale distribution of MAGL in astrocytes 45
4.3.1. Demonstrating the expression of MAGL in CA1 hippocampal astrocytes 45
4.3.2. The distribution of MAGL in hippocampal astrocytes suggests a synapse-independent role 48
5. Discussion.....52
5.1. Nanoscale visualization of astrocytes labeled by electroporation 52
5.2. Dual-color STORM imaging of astrocytes in brain tissue 54
5.3. Investigating the spatial distribution of astrocytic MAGL 55
6. Conclusions 59
7. Summary.....61
8. References 62
9. Bibliography of the candidate's publications 77
10. Acknowledgements 79

List of abbreviations

2-AG - 2-arachidonoyl-glycerol

AA - arachidonic acid

AF647 - Alexa Fluor 647

CA1 - cornu Ammonis 1

CB_1 - type 1 cannabinoid receptor

ΔnCdh2 - dominant-negative form of N-cadherin

ChR2 - Channelrhodopsin-2

COX - cyclooxygenase enzyme

cPLA2 - cytosolic phospholipase A2

DAPI - 4',6-diamidino-2-phenylindole

DBSCAN - density-based spatial clustering of applications with noise

E14.5 - embryonic day 14.5

ECS - endocannabinoid system

Fig. - Figure

FWHM - full width at half maximum

GFAP - glial fibrillary acidic protein

GFP - green fluorescent protein

GLT-1 - excitatory amino acid transporter (glial glutamate transporter)

GS - glutamine synthetase

IQR - interquartile range

IUE - *in utero* electroporation

KO - knockout

LP - localization point

LPS - lipopolysaccharide

MAGL - monoacylglycerol lipase

mRNA - messenger ribonucleic acid

NLP - number of localization points

norm. - normalized

NND - nearest neighbor distance

P1 - postnatal day 1

PALE - postnatal astrocyte labeling by electroporation

PALM - photo-activated localization microscopy

PAP - perisynaptic astrocytic process

PSF - point-spread function

RGPC - radial glial progenitor cell

ROI - region of interest

SEM - standard error of the mean

SMLM - single-molecule localization microscopy

SRM - super-resolution microscopy

STED - stimulated emission depletion microscopy

STORM - stochastic optical reconstruction microscopy

THC - delta-9-tetrahydrocannabinol

WT - wild type

1. Introduction

The brain is arguably one of the most complex organs of mammals. Recent high-throughput RNA-sequencing studies not only revealed that hundreds of different cell types exist in the mouse, but also how the molecular make-up can drive cellular diversity and ultimately neuronal function[1]. However, RNA counts often do not correlate with protein abundance, and also lack spatial information, whereas it is well known that proteins can fulfil different functions in distinct subcellular compartments, cellular states, or when interacting with other proteins. Therefore, knowing the precise distribution of proteins is key to understanding the function of any cell type.

1.1. Super-resolution imaging as a way to overcome the diffraction barrier

Traditionally, life science researchers had to choose between utilizing either electron microscopy or fluorescence light microscopy for the examination of protein distributions. While electron microscopy offers the requisite resolution to reveal precise subcellular distributions alongside cellular ultrastructure, it also suffers from serious drawbacks. The required specific and laborious sample preparation steps not only limit its routine applicability but also impede achieving high labeling densities, and therefore sparse molecular targets might remain undetected. Furthermore, anisotropic distortions in the tissue can give rise to artifacts, leading to erroneous spatial analyses. The capacity for multiplexing is also restricted, making it often impossible to assign molecular data to identified cell types or synapses. Lastly, and perhaps most importantly, live samples and therefore dynamic molecular changes cannot be investigated[2].

Fluorescent light microscopy, on the other hand, is virtually free from the above-mentioned limitations, making it suitable for live imaging, offering versatile multiplexing capabilities, and being user-friendly and easily automated. However, it faces its own critical drawback – its resolution is constrained by light diffraction, resulting in a resolution limit of approximately 250 nm laterally and 450 nm axially. This limitation hinders detailed examination of crucial cellular structures, including synapses, which have dimensions one order of magnitude smaller than the resolution limit. Key elements like the synaptic cleft (20-40 nm), synaptic vesicles (~40 nm), and postsynaptic density (around 300 ± 150 nm) all fall below the achievable resolution[3]. In addition to synapses,

the dimensions of various other cellular elements, including dendritic spines, thin astroglial filaments, and organelles like mitochondria, also fall below the diffraction limit.

In the early 21st century, life science researchers were able to bridge the gap between electron and fluorescence light microscopy with the development of various super-resolution microscopic (SRM) techniques[4]. These techniques, awarded the Nobel Prize in Chemistry in 2014, retained the versatility of fluorescence microscopy while significantly improving resolution, often reaching a few tens of nanometers. SRM methods fall into two main categories: targeted (deterministic) and stochastic (probabilistic) (Fig. 1). Targeted methods, like stimulated emission depletion microscopy (STED), enhance resolution by effectively shrinking the point-spread function (PSF) of the microscope. To achieve this, STED utilizes a second, doughnut-shaped depletion beam that is superimposed onto the primary excitation beam and deactivates fluorescence at the periphery, leaving only a smaller spot free for fluorescent emission. While theoretically there is no upper limit for the resolution gain, practical considerations like photobleaching or phototoxicity constrain the effective PSF size of STED to around 30-80 nm, depending on the microscopic design[4]. As the resulting super-resolution image is a pixel-based image like the output of other common microscopic imaging modalities, STED images can be effectively analyzed and visualized with widely used software tools.

Stochastic methods utilize a markedly different approach to create a super-resolved image. They rely on the fact that the position of a single emitter can be determined with high precision by simply finding the center of the single-molecule image. The uncertainty in this step, typically involving fitting Gaussian curves onto the camera image, primarily depends on the PSF size and the number of collected photons. Single molecules were imaged as early as the 1990s, but this does not translate to super-resolution imaging of biological samples with millions of emitters. The overlapping emissions create a blurred image, making it impossible to extract molecular coordinates through mathematical means. The crucial step is to control the states of emitters to ensure that only one emitter is active in a diffraction-limited area at a given time point. After determining their center coordinates, these emitters should become inactive, and other, so-far inactive emitters should then be activated. By iterating this process called "blinking", the positions of all emitters can be retrieved with single-molecule precision[5,6]. This temporal separation is common to all stochastic methods, which differ mainly in

how they achieve the two different (commonly called on/off or bright/dark) states of emitters - STochastic Optical Reconstruction Microscopy (STORM)[7] employs photoswitchable small organic fluorophores attached to antibodies, Photo-Activated Localization Microscopy (PALM)[8] relies on photoswitchable fluorescent proteins, while DNA-PAINT[9] utilizes the spontaneous binding and unbinding of dye-coupled DNA oligomers to their respective counterparts on the target molecules.

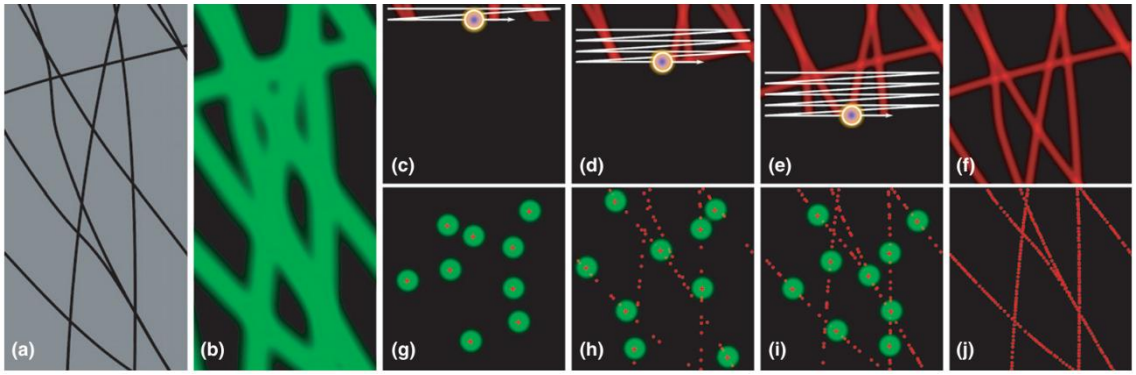


Figure 1. Comparison of STED and STORM imaging acquisition strategies. *(a) Simulated example of closely spaced filaments with features extending beyond the diffraction limit. (b) Conventional fluorescence microscopy results in a diffraction-limited image, obscuring the underlying biological structure. (c–f) STED imaging generates a super-resolved image via point-by-point scanning by shrinking the point spread function. (g–h) STORM imaging sequentially localizes individual molecules over time to reconstruct a pointillistic super-resolution image. Figure adapted from Tam and Merino, 2015[10].*

As stochastic approaches localize individual molecules, they are often referred to as Single-Molecule Localization Microscopy (SMLM) techniques. Their biggest advantage lies in their name, that is, they are endowed with single-molecule sensitivity. Hence, they can also reveal molecular heterogeneities and are well suited to study the spatial characteristics like clustering patterns of molecules. The output of these modalities, however, is only a list of molecular coordinates, and therefore they require different software tools to analyze and to visualize the data. Moreover, many strengths of SMLM methods like counting molecules or defining true cluster sizes need careful calibration or control measurements for valid data interpretation[11]. Nevertheless, the relatively easy instrumentation makes SMLM methods increasingly popular[6].

The choice of the optimal super-resolution technique should be guided by the specific biological questions to be addressed[12,13]. STED imaging is more suitable for capturing dynamic changes, owing to its fast scanning speed that enables super-resolved video-rate imaging. SMLM, on the other hand, with its ability to localize individual molecules offers even greater resolution and sensitivity, and can also unveil molecular heterogeneities. With ongoing technological developments, however, the boundaries between these technologies are anticipated to diminish. The concept of MINimal photon FLUXes (MINFLUX) microscopy, achieving true molecular resolution at the scale of 1-5 nm, emerged from the fusion of these two main branches of SRM modalities[14].

1.2. SMLM imaging in neuroscience research

The emergence of super-resolution microscopic methods nearly two decades ago has significantly advanced our understanding of the spatial distribution of molecules and their impact on neuronal function, particularly at the synaptic level. Here, I aim to highlight a few examples illustrating the strength of SRM in neuroscience research, with an emphasis on SMLM imaging[2,15,16].

The first seminal SMLM study on fixed brain tissue sections was published in 2010[17]. In this study, cortical and olfactory bulb synapses were visualized by simultaneous labeling of the postsynaptic scaffold protein Homer and presynaptic cytomatrix protein Bassoon. When these targets were positioned in a side view (i.e., trans-synaptic axis rotated into the viewing plane), they could be clearly separated, despite mean distances between localization points being approximately 150 nm. By using these two targets as a reference plane and imaging distinct molecules (or distinct epitopes of the same molecule) as a third target, an axial map of synaptic proteins across the synaptic cleft could be generated. This revealed that while postsynaptic proteins are organized in a laminar manner, presynaptic proteins tend to localize rather axially relative to the cleft.

Shortly after, PALM experiments conducted on neuronal cultures revealed an uneven distribution of numerous postsynaptic scaffold molecules, including PSD-95, Shank3, or Homer1c. These molecules exhibited a variable number of denser clusters termed nanodomains within the postsynaptic density (PSD)[18]. These nanodomains, approximately 50-80 nm in size, displayed a molecular density around 3.5 times higher than their surroundings. Notably, they selectively concentrated AMPA-type glutamate

receptors while excluding NMDA-type receptors, despite both receptor types forming nanodomains of roughly similar sizes[19,20].

Presynaptic scaffolding molecules within the active zone, such as Bassoon, RIM1/2, and Munc13, also exhibit a tendency to form clusters. Additionally, these pre- and postsynaptic scaffolding nanodomains align in a trans-synaptic manner, forming "nanocolumns" that optimize the distance between vesicle fusion sites and clusters of neurotransmitter receptors[21]. This columnar organization is subject to activity-dependent modulation, where long-term potentiation or depression bidirectionally influences the alignment of trans-synaptic nanodomains, subsequently impacting synaptic strength at a diffraction-limited, sub-synaptic scale. Importantly, this clustering behavior is not exclusive to glutamatergic synapses: Gephyrin and $GABA_A$ receptors on the postsynaptic side of inhibitory synapses also form sub-synaptic domains[22], and dopamine transporters create nanodomains in a cholesterol-dependent manner in dopaminergic neurons[23].

The majority of the aforementioned studies were conducted using cell culture systems, providing insights into an "average" synapse but lacking the cellular diversity inherent to the brain. To understand how molecular diversity drives cellular and physiological diversity, it is essential to perform molecular imaging within intact brain tissue in a cell type-specific manner. STORM imaging by itself, however, does not reveal the cellular context from which the data were gathered. Therefore, to interpret the molecular data within its respective cellular and subcellular context, we have recently developed an approach integrating physiological, morphological, and nanoscale molecular measurements[24,25]. This method enabled us to demonstrate that the differential endocannabinoid signaling between perisomatically and dendritically projecting interneurons may be attributed to distinct active zone compositions, and consequently, distinct control of CB_1 cannabinoid receptors over their main effectors, the voltage-gated calcium channels[25].

The crucial step in our method was to correlate the output of two distinct microscopic modalities: the coordinate-based molecular information gathered by STORM and the pixel-based contextual information obtained by confocal microscopy. The contextual information can be provided by various means, such as biocytin filling of cell types identified in electrophysiological recordings, cell type-specific expression of genetically encoded fluorescent proteins, labeling via electroporation or viral injection,

as well as immunolabeling against cellular or subcellular markers. A confocal image with up to four channels enables the identification of specific niches at the best resolution that can be obtained via conventional light microscopic techniques, while the STORM image of the protein of interest provides much more detailed molecular information. We summarized all the key steps in our protocol on how to obtain such images, and created a software tool named VividSTORM to easily align and analyze these two distinct microscopic modalities in a correlative manner[24]. More recently, we also provided some important considerations and useful tips for optimal STORM imaging in brain tissue samples, with an emphasis on analyzing CB_1 receptors in GABAergic terminals[26] (Fig. 2).

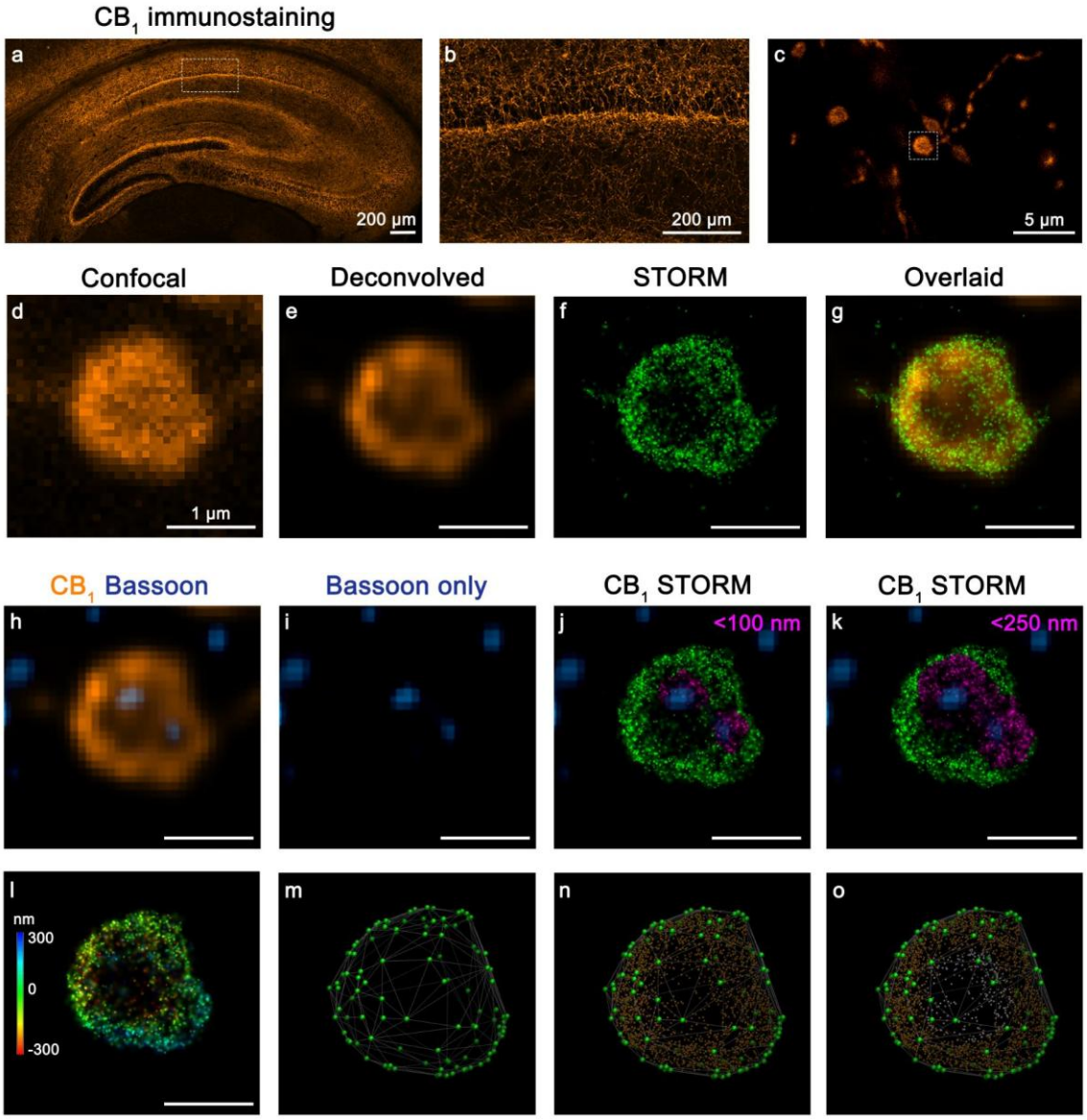


Figure 2. Multiscale visualization of CB_1 receptors in mouse brain tissue. *(a) Immunostaining against CB_1 shows the well-known characteristic staining pattern of cannabinoid receptor distribution in the CA1 hippocampal region. (b) Zoomed-in view of the rectangle in (a). Dense meshwork of axons belonging to GABAergic interneurons is easily discernible. (c) Higher magnification shows the axon terminals along individual axons. (d) Enlarged view of an axon terminal (bouton) from the boxed region in (c) imaged via confocal microscopy. (e) The signal-to-noise ratio is significantly improved after deconvolution. However, the information content that can be retrieved from this image is still limited by the diffraction of light. Deconvolution was done using the Huygens SVI software. (f) STORM image from the very same region shows individual CB_1 localization points at nanometer resolution and better captures the distribution of*

the protein along the surface of the bouton. Localization points are rendered as Gaussian distributions in the NIS-Elements N-STORM module. (g) STORM image overlaid onto the deconvolved confocal image. (h) Deconvolved confocal image of CB_1 along with the active zone marker protein Bassoon (in blue). (i) Visualization of Bassoon shows that there are two active zones in this axon terminal. (j) STORM localization points are colored based on their proximity to thresholded Bassoon-positive pixels (less than 100 nm in magenta; more than 100 nm in green). Thresholding was done via the Otsu method. VividSTORM[24] was used to align the respective STORM and confocal images of CB_1 onto each other and to determine the offset between the two imaging modalities. STORM localization points were filtered to the ones belonging to the bouton. (k) Same as (j) but using 250 nm as a distance threshold. (l) STORM localization points color-coded by their position along the axial axis. The color bar is shown on the left. (m) Convex hull representation of the localization points allows the approximation of the bouton surface. The illustration was done using Visual Molecular Dynamics software, showing the outermost localization points (i.e., vertices of the convex hull) as atoms and the convex hull edges as chemical bonds. (n) Inner localization points not forming the convex hull vertices are shown as smaller golden spheres. (o) The centermost (possibly internalized) localization points colored in gray were determined by calculating the distances of all localization points to the closest convex hull surface and applying a distance threshold. VividSTORM software was used for the distance calculation[24,25]. The scale bars in panel (e–l) are the same as for panel (d). Figure reproduced from Zöldi and Katona, 2023[26] .

It is important to note that during correlative imaging, the fidelity with which we assign localization points to the profile of interest depends on the resolution of the correlative method and on the precision of alignment. This means that although STORM data provides nanoscale information at an unprecedented resolution, one cannot, for example, filter the localization points onto the cellular context with better precision than the resolution of the confocal image. This problem is negligible when imaging abundant targets such as CB_1 receptors that cover the whole surface of GABAergic boutons where cellular boundaries can be easily seen from the STORM datapoints and where the profile size is much larger than the diffraction limit[25,26]. However, when the cellular context is below the diffraction limit such as thin astrocytic processes in the range of a few tens to a few hundred nanometers, and when scarce localization point data cannot provide any

visual clues, correlative imaging suffers from serious drawbacks. In these cases, dual-color STORM imaging is preferred to maintain a nanoscale resolution both for the molecular data and for the anatomical context.

1.3. A growing demand for imaging astrocytic proteins at the nanoscale level

Astrocytes were traditionally perceived solely as supportive cells to neurons, playing an indispensable yet seemingly passive role in the modulation of brain functioning. However, with the advent of the "tripartite synapse" perspective[27], which elevates astrocytes to equal standing with neurons, extensive research has revealed that glia actively serve as modulators of information processing. Indeed, astrocytes play a crucial role in overseeing nearly every aspect of brain functioning, influencing synaptic communication, network oscillations, and the regulation of cerebral blood flow, energy metabolism, brain homeostasis, as well as the course of neuroinflammation[28,29]. It is therefore not surprising that astrocytes have emerged as key targets for various therapeutic interventions, including neurodegenerative disorders[30–32].

Although mapping the precise distribution of proteins should be one of the first steps to understand drug mechanisms and to avoid unwanted side effects, investigating protein distributions in astrocytes lags behind that of neurons[33,34]. The highly complex morphology of astrocytes with thousands of processes well below the diffraction limit poses an exceptional challenge to perform molecular imaging inside astrocytes, as even the proper delineation of these cellular structures requires super-resolution imaging modalities[35–37]. Therefore, visualizing the cellular context by confocal microscopy[24] is not suitable, as the fidelity of assigning localization points to the cellular profile depends on the resolution of the correlated imaging modality and on the precision of the alignment, both of which introduce bigger errors than the spatial dimensions of such processes. Of note, the majority of calcium transients that define the functional output of astrocytes occur in these fine processes[38].

Another challenge is the use of tissue preparations instead of cell culture systems. Astrocytes in culture adopt very different morphologies compared to the ones in their native cellular context, being regarded more as an inflammatory (“reactive”) phenotype with unique molecular signatures[39,40]. Moreover, recent RNA-seq studies revealed that astrocytes are heterogeneous and multiple molecularly distinct subtypes exist whose

ratios also change in certain disease conditions[41,42]. Therefore, molecular profiling in cell culture will not only miss the molecular spectrum of astrocytes but might also provide non-physiological data. To date, SMLM is predominantly employed in cell culture systems, where minimal fluorescent background, low light scattering, and negligible depth-dependent microscopic aberrations facilitate super-resolution imaging. Lastly, many of the astrocytic transcripts and proteins appear to have very low copy numbers[43,44], favoring the use of highly sensitive methods such as SMLM.

Due to the aforementioned challenges, it is not surprising that only a handful of studies applied SMLM in astrocyte research. One of the first ones addressed the question of whether astrocytes translate mRNAs locally in perisynaptic astrocytic processes (PAPs)[45]. Astrocytic ribosomes were visualized by using a transgenic mouse line where a ribosomal protein (RPL10A) is fused to Enhanced Green Fluorescent Protein (EGFP) under the astrocyte-specific promoter Aldh1L1. As PAPs lack specific markers for their identification, Bassoon and Homer were also labeled to identify astrocytic ribosomes that are close to synapses and hence are presumably in PAPs. Three-color STORM imaging of the synaptic markers and EGFP demonstrated that many of the ribosomes are indeed closer than 100 nm to the synaptic structures. Of note, these pioneering multi-color STORM images utilized the so-called "activator-reporter" method[17], which due to its high rate of channel-crosstalk is only suitable for revealing non-overlapping structures.

The group of Dmitri Rusakov utilized spectrally distinct fluorophores for multi-color STORM imaging and showed both in culture and brain tissue that the glial fibrillary acidic protein (GFAP) labels a much more restricted portion of the astrocytic territory compared to other astrocytic markers such as S100β or glutamine synthetase (GS), which are present in glial processes that are thinner than the diffraction limit[46,47]. They also demonstrated that the surface expression of the main glial glutamate transporter GLT-1 and its clustering behavior relies on its C-terminus, as its deletion shifted the GLT-1 localizations more distant from synapses labeled by PSD-95[48]. GLT-1 nanoscale distances to synapses were also altered during long-term potentiation due to the withdrawal of PAPs[49]. These seminal studies captured only abundant proteins that are specific to astrocytes, and therefore there was no need to assign localization points to the cell or structure of interest. Identifying astrocytic proteins that are present in multiple cell types, however, would require the delineation of the astrocytic arbor.

STED microscopy was employed to achieve higher-resolution imaging of astrocytic architecture, revealing that astrocytic filaments consist of alternating thinner, filamentous regions (shafts) and wider, bulbous segments (nodes). Nodes are thought to function as structural units that compartmentalize astrocytic signals, akin to dendritic spines in neurons[50]. Although the astrocytic nanoarchitecture formed ring-like structures, these rings are likely separated by membranes, with STED's limited axial resolution potentially creating the false appearance of continuity[51,52]. Despite this limitation, STED microscopy allows for much more reliable quantification of astrocytic structural details and their changes under specific perturbations compared to confocal microscopy[51,53].

1.4. Monoacylglycerol lipase, a promising enzyme at the crossroads of endocannabinoid and prostaglandin signaling

Feedback mechanisms are pivotal for the precise control of any biological signaling system. In the brain, one of the main regulatory feedback mechanisms is the retrograde endocannabinoid signaling which fine-tunes the synaptic transmission between various cell types in multiple brain regions[54]. The term endocannabinoid is a short form for endogenous cannabinoids, molecules that are produced by the brain and have similar effects to exogenous cannabinoids such as the main psychoactive component of marijuana, delta-9-tetrahydrocannabinol (THC). The endocannabinoid system (ECS) is composed of synthesizing and degrading enzymes for endocannabinoids, as well as the molecular targets of THC, the cannabinoid receptors[55].

The principal components of the ECS are positioned in a way that is optimal for a retrograde signaling route. The main synaptic endocannabinoid, 2-arachidonoyl-glycerol (2-AG), is produced on-demand by the postsynaptically located diacylglycerol lipase alpha (DAGLα) enzyme and exerts its effect via the presynaptically located CB_1 cannabinoid receptors, which ultimately leads to the inhibition of voltage-gated calcium channels and hence to decreased synaptic transmission. Finally, the action of endocannabinoids is terminated by the presynaptically located monoacylglycerol lipase (MAGL) enzyme[55,56]. Besides this archetypical signaling route, however, there are many more players of the endocannabinoid system, including distinct receptors, interacting proteins, enzymes, ligands, and cell types, that all contribute to the various cell- and synapse-specific actions of the ECS[54].

The ECS is a rapidly growing field of neuroscience research, not only because of its relevance due to the ever-continuing legalization of marijuana in various countries and states, but also because of its great therapeutic potential to treat as diverse diseases as anxiety, depression, epilepsy, or metabolic diseases. Rimonabant, a CB_1 receptor antagonist, had promising therapeutic potential to treat obesity via peripheral cannabinoid mechanisms, but it was soon withdrawn from the market because of its serious psychiatric side effects[57]. Endocannabinoid action, however, may be modulated at the level of degrading enzymes. A selective inhibitor of MAGL named JZL184 recapitulated three of the four main behavioral effects induced by CB_1 agonists (that is analgesia, hypomotility, hypothermia and catalepsy, collectively referred to as the tetrad test for cannabinoid activity)[58]. This strong effect can be attributed to the fact that in the brain ~85% of 2-AG hydrolase activity can be ascribed to MAGL[59]. Interestingly, the high preference toward 2-AG regulation by MAGL is specific to the brain as in other tissues MAGL inhibition causes alterations in the levels of other monoacylglycerols, with little or no change in 2-AG levels[60]. The reason behind this specificity is not fully understood but might be therapeutically exploitable to selectively change endocannabinoid levels in the brain.

A groundbreaking study from the lab of Benjamin Cravatt expanded the role of MAGL. They showed that by degrading 2-AG into arachidonic acid (AA), MAGL also produces the precursors for subsequent prostaglandin synthesis, mechanistically coupling endocannabinoid signaling to the inflammatory prostaglandin pathway in the brain[61]. This was unexpected, as in most tissues the source of this AA pool is generated mainly by the cytosolic phospholipase A2 (cPLA2) enzyme. However, in the brain, only mice deficient for MAGL, but not for cPLA2, had reduced AA and prostaglandin levels. Notably, this coupling of lipid mediators is more pronounced in inflammatory settings, such as when mice are challenged with the bacterial proinflammatory agent lipopolysaccharide (LPS)[61].

Interestingly, subsequent studies using cell type-specific MAGL knockout animals revealed that the enhanced prostaglandin production upon inflammatory conditions is mediated via astrocytic, but not neuronal, MAGL, and only astrocytes are capable of coupling elevations in 2-AG with reductions in AA and prostaglandin levels[62]. Therefore, a new hypothesis has emerged, postulating that the main producers of prostaglandin in the brain are astrocytes, using 2-AG generated either by neurons or by themselves in basal or inflammatory conditions, respectively[62]. Knocking out MAGL

specifically from astrocytes not only reduced LPS-mediated inflammation[63], but turned out to be neuroprotective in traumatic brain injury[64] and Huntington's disease[65] mouse models. Cell type-specific knockout mice had the additional benefit of not producing behavioral tolerance to cannabinoid agonists[62], unlike mice where MAGL was inactivated globally either by genetic disruption or repeated inhibitor treatment[66].

Prostaglandins are important proinflammatory molecules throughout the body that are produced from AA by the cyclooxygenase enzymes (COX1 and COX2). As COX1 and COX2 inhibitors have gastrointestinal or cardiovascular side effects, respectively, MAGL inhibitors emerged as a promising therapeutic strategy to control inflammation in the brain[67,68]. MAGL inhibition proved to be beneficial in mouse models of Parkinson's[61] and Alzheimer's disease[69,70], as well as postictal ischemia[71]. Notably, MAGL inhibitors are in the pipeline of the global pharmaceutical company Lundbeck to treat chronic pain, epilepsy, and other potential neurological disorders accompanied by neuroinflammation[i,ii].

How MAGL achieves its functional versatility remains elusive. Elucidating the precise subcellular distribution of MAGL could shed light on whether there are separate pools of this enzyme that may regulate endocannabinoid or prostaglandin signaling. Apart from the dentate gyrus astrocytes[72] and the special Bergmann glia in the cerebellum[73] where MAGL expression is so high that it can be detected at the light microscopic level, MAGL in hippocampal and neocortical astrocytes has remained below the detection threshold in electron microscopy studies[74,75]. Hence, technical limitations have thus far prevented deeper insights into the role of astrocytic MAGL. This would be of primary interest as endocannabinoid signaling in astrocytes is an exciting and rapidly advancing area of neuroscience with potential implications for treating various neurological disorders[76].

[i] https://www.lundbeck.com/global/our-science/pipeline;
[ii] https://www.lundbeck.com/content/dam/lundbeck-com/masters/global-site/global-site/investors/r-d-event-london/RD%20day%202023%20London_compiled_FINAL_web.pdf

2. Objectives

Interfering with MAGL activity holds great therapeutic potential in the treatment of many neurological disorders. Examining the precise subcellular distribution of MAGL, its association with other synaptic elements, organelles, or proteins of certain pathways, could help our understanding of the role of MAGL in health and disease. With the current toolsets, however, the visualization of astrocytic MAGL pools and their differentiation from presynaptic pools in mouse brain tissue sections is challenging. Therefore, in this study, we aimed to develop a methodology by which glial proteins, and ultimately MAGL, can be studied in individual astrocytes at the nanoscale level using STORM.

This requires a labeling strategy that sparsely and selectively labels individual astrocytes, allowing for the complete nanoscale reconstruction of their intricate arbor. Our first specific aim was to test if electroporation could serve as a suitable method, applying it both *in utero* and postnatally to target developing radial glial cells and hippocampal astrocytes, respectively. We reasoned that a membrane-targeted fluorescent protein could not only visualize the finest astrocytic processes but could immediately inform us about the success of electroporation. By immunolabeling the fluorescent protein with an antibody carrying a STORM-compatible dye, the astrocytic processes could be resolved with nanoscale resolution.

Our second goal was to demonstrate that dual-color STORM imaging has the power to faithfully discriminate between astrocytic and neighboring synaptic proteins, localizing only the former but not the latter in the super-resolved filaments. We reasoned that a prerequisite of such discrimination is to have perfect alignment of the two microscopic channels, and not to detect any crosstalk between them. We hypothesized that the recently developed tessellation approaches and molecular distance calculations could be robust tools to retrieve those measures.

Lastly, we aimed to explore the spatial expression pattern of MAGL in hippocampal CA1 astrocytes, whether it is preferentially enriched in close proximity to synapses or rather follows a random distribution. To exclude the possibility that nonspecific labeling is evaluated as a scarce astrocytic MAGL signal, images taken from MAGL knockout animals would serve as a control to determine the background labeling density in astrocytic filaments.

3. Methods

The methods are reproduced from Zöldi and Katona, 2026[77] , except for the embryonic experiments, which are adapted from László et al., 2020[78].

3.1. Animals

Animal experiments were approved by the Hungarian Committee of the Scientific Ethics of Animal Research (license number: PE/EA/201-7/2020) and were carried out according to the Hungarian Act of Animal Care and Experimentation (1998, XXVIII, Section 243/1998, renewed in 40/2013), which is in accordance with the European Communities Council Directive of November 24, 1986 (86/609/EEC; Section 243/1998). Mice were kept under approved, specific-pathogen-free laboratory conditions, and all efforts were made to minimize pain and to reduce the number of animals used. To develop the methodology for the PALE approach and astrocyte-specific STORM imaging in the CA1 subregion of the hippocampus, we used male and female CD-1 mice (ranging in age from 29 to 155 days; Charles River Laboratories Hungary). To study the nanoscale distribution of MAGL and to verify the specificity of the MAGL antibody, we used male *Mgll*$^{+/+}$ and *Mgll*$^{-/-}$ littermates (age: 100–166 days, kindly provided by Prof. Kenji Sakimura, Niigata University) that were kept on a C57BL/6N background. Mice were bred and genotyped as previously described[72]. RNAscope experiments utilized 60–66-day-old mice from a distinct MAGL line[66], which was generously provided by Prof. Benjamin F. Cravatt (The Scripps Research Institute) and Prof. Anna Kalinovsky (Indiana University). These specific procedures were approved by the Institutional Animal Care and Use Committee (IACUC) of Indiana University (protocol number: 21-015) and conform to the National Institutes of Health Guidelines on the Care and Use of Animals.

The *in utero* electroporation experiments were approved by the Hungarian Committee of the Scientific Ethics of Animal Research (license numbers: XIV-1-001/2332-4/2012 and PE/EA/354-5/2018) and were carried out according to the same regulations. Both male and female embryos were used. C57BL/6 and CD-1 mice were obtained from Charles River Laboratories.

3.2. *In utero* electroporation

In utero electroporation was carried out as described previously[78]. The dominant-negative form of N-cadherin (ΔnCdh2) was generated from mouse N-cadherin (*Cdh2*), cloned by RT-PCR from E16.5 brain cDNA, by OliI–HindIII digestion, Klenow fill-in of the HindIII overhang and religation. The resulting construct, validated by sequencing, encodes a truncated N-cadherin that contains the signal sequence followed by the transmembrane and intracellular domains but lacks the extracellular domain. ΔnCdh2 was subcloned into the bicistronic pCAGIG mammalian expression vector carrying an internal ribosome entry site (IRES)-GFP cassette (a gift from Connie Cepko, Addgene #11159); the empty pCAGIG vector expressing GFP alone served as control.

Timed-pregnant female mice were anesthetized with Avertin (1.25% v/v, Sigma), and the uterine horns were exposed. The plasmid (1–2 μg/μL at 1 μL volume) in endotoxin-free water containing Fast Green (1:10,000, Roth) was injected into the lateral ventricle of the embryos via a glass capillary at embryonic day 14.5 (E14.5). Electroporation was performed with tweezer electrodes (5 pulses of 40 V for 50 ms at 950 ms intervals) using an SP-3c electroporator (Supertech). After electroporation, the uterine horns were returned into the abdominal cavity, the wall and skin were sutured, and the embryos were allowed to continue their development.

3.3. Preparation and labeling of embryonic brain sections

Embryonic brains were immersion-fixed with 4% PFA overnight at 4°C. For confocal imaging, brains were cryoprotected in 15% sucrose in PBS for 15 min and then in 30% sucrose overnight at 4°C, embedded into Tissue-Tek Optimal Cutting Temperature compound (Sakura), and 20-μm-thick cryosections were collected on Superfrost Ultra Plus glass slides (ThermoFisher) and treated again with 4% PFA for 10 min. After several PBS washes, sections were permeabilized with 0.2% Triton X-100 in PBS and blocked with 1% human serum albumin (Sigma) in PBS for 1 h. To visualize F-actin-enriched adherens junctions at the ventricular wall, sections were incubated with the high-affinity F-actin probe Alexa Fluor 568-Phalloidin (1:500, ThermoFisher) for 2 h at room temperature. Slides were then washed with PBS, mounted with Vectashield Hardset Antifade Mounting Medium (Vector), covered and sealed with nail polish.

For STORM imaging, brains were fixed in the same manner and cut into 20-µm-thick sections, which were immunostained in a free-floating manner. Sections were permeabilized with 0.2% Triton X-100 in PBS, blocked with 5% normal donkey serum (Sigma) in PBS for 1 h, and incubated with a mouse antibody to nestin (1:200, Millipore, MAB353) overnight at 4°C. After intensive washing in PBS, sections were incubated with Alexa Fluor 647-conjugated donkey anti-mouse secondary antibody (1:400, Jackson) for 4 h. Instead of glass slides, sections were dried onto coverslips and stored uncovered at 4°C until STORM imaging.

3.4. Postnatal astrocyte labeling by electroporation (PALE)

Newborn and postnatal day 1 (P0–P1) pups were sedated by hypothermia. Glass capillaries were pulled by a micropipette puller (Sutter Instrument, Novato, CA, USA) and were filled with plasmid DNA solution (diluted in endotoxin-free water to 1 µg/mL concentration). Injection was delivered into one of the lateral ventricles of the pups. Using mouth aspirator tubes (Sigma-Aldrich, A5177), 1–2 µL of plasmid solution was administered into the ventricles. The non-toxic Fast Green dye (1:10,000; Roth) was added to the solution to visualize the crescent-shaped ventricle and to determine the success of the injections. Electroporation was performed with tweezer electrodes using an SP-3c electroporator (Supertech, adjusted to 5 pulses of 100 V for 50 ms at 950 ms intervals). The negative terminal of the electrode was placed above the site of injection, while the positive terminal was placed to the opposite side of the head, below the pup's chin. The two terminals of the electrodes were slightly rotated during electroporation to ensure a homogeneous labeling of the entire CA1 region of the hippocampus. For targeting neocortical astrocytes, the electrode polarity was reversed. After electroporation, the pups were placed onto a thermal heating pad until their skin color recovered and then were returned to their dams. When performing PALE on two consecutive days, the same procedure was repeated on P0 and P1 on the same pups. No pups died because of the electroporation procedure. Electroporation on P2 did not achieve the “useful density” of PALE-labeled astrocytes. We defined “useful density” as at least 10 astrocytes per 20-µm-thick section. The extent of labeled astrocytes along the transverse axis of the hippocampus (i.e., along the CA1–CA3 trajectory) spanned a mean of 1962 µm (SD = 380 µm). The range of successfully labeled astrocytes along the rostro-

caudal axis in adjacent sections was approximately 1000–1500 μm. Expression of the injected construct was observed as early as P5, and expression levels remained high up to 227 days of age, the oldest time point investigated in this study.

3.5. DNA constructs

The following constructs were used: pAAV-GFAP104-ChR2-mCherry plasmid (Addgene #58892); CAG-ChR2-GFP (Addgene #26929); Lck-GFP (Addgene #61099); and GFAP-EGFP (Addgene #50473). The constructs visualized a similar number of astrocytes with comparable morphological features. Because radial glia primarily differentiate into astrocytes around the time of birth, the use of astrocyte-specific promoters is not strictly required for postnatal electroporation to achieve cell type-specific targeting. ChR2 was not used for optogenetic activation of astrocytes; it only served (similarly to the Lck tag) to ensure the integration of the fluorescent protein-containing construct into the plasma membrane. We preferred mCherry over GFP to visualize astrocytes, as mCherry could be more easily bleached. This allowed us to reuse the same spectral channel for STORM imaging with the STORM-compatible CF568 dye.

3.6. Preparation of hippocampal sections

Two approaches were used in this study. The two tissue preparation methods did not result in notable differences in the immunolabeling pattern. In the first approach, mice were deeply anesthetized with an intraperitoneal injection of Avertin (1.25% v/v, Sigma-Aldrich) and were perfused transcardially with 0.9% saline for 2 min and then with 4% paraformaldehyde (PFA, TAAB, P001) dissolved in 0.1 M phosphate buffer (PB, pH = 7.4 containing Na_2HPO_4, Sigma-Aldrich, 304305 and NaH_2PO_4, Sigma-Aldrich, 71500) for 20 min using a peristaltic pump at 5 mL/min speed. Brains were removed from the skull and postfixed overnight in 4% PFA. Hippocampal coronal sections were cut on a Leica VT-1200S vibratome at thicknesses of 20 μm for STORM imaging and 50 μm for confocal microscopy.

In the second approach, acute hippocampal slices were prepared in the same manner as the traditional approach in *ex vivo* electrophysiological experiments. Briefly, mice were deeply anesthetized by isoflurane. The brains were quickly removed from the skull and transferred to ice-cold sucrose-containing artificial cerebrospinal fluid (ACSF,

containing in mM: 75 NaCl, 75 sucrose, 2.5 KCl, 25 glucose, 1.25 NaH_2PO_4, 4 $MgCl_2$, 0.5 $CaCl_2$, 24 $NaHCO_3$, Sigma-Aldrich, St. Louis, MO, USA) equilibrated with 95% O_2 and 5% CO_2. The 300-µm-thick coronal hippocampal acute slices were cut using a Leica VT-1200S vibratome. Slices were pre-incubated at 34°C in sucrose-containing ACSF for 1 h. Afterwards, the slices were placed into 4% PFA for overnight immersion fixation at 4°C, and the next day the fixative was changed to 0.1 M PB. To determine the success of the electroporation, slices were mounted onto a microscopic glass slide, covered by a coverslip, and placed under an upright microscope (Nikon Eclipse 80i, equipped with a DS-Fi1 CCD camera). Slices containing a suitable number of astrocytes were re-embedded in 2% agarose and cut on a vibratome to 20-µm-thick sections. We found the acute slice method better than the perfusion-based approach for selecting the most suitable sections. In addition, fixation quality during perfusion introduces additional variability in immunolabeling efficiency. Therefore, the acute slice approach was used in case of comparison of immunolabeling obtained from *Mgll*$^{+/+}$ and *Mgll*$^{-/-}$ littermate mouse hippocampi.

3.7. Immunolabeling

Immunolabeling of hippocampal sections was carried out in a free-floating manner in 24-well tissue culture plates (Greiner Bio-One CELLSTAR, 662102), gently rotated on orbital shakers (Biosan OS-10). Sections were blocked and permeabilized with 5% normal donkey serum (NDS) and 0.3% Triton in Tris-buffered saline (TBS, pH = 7.4, 0.05 M, containing Trizma hydrochloride, Trizma base and NaCl) for 45 min. Sections were incubated overnight at 4°C in primary antibody solution diluted in TBS. After washing the sections 3 times 10 min in TBS, incubation in the respective secondary antibody solution was carried out for 4 h. For primary and secondary antibodies and their concentrations, see Table 1. Sections were washed again 3 times for 10 min in TBS, then in 0.1 M PB. For confocal imaging, sections were mounted on glass microscope slides with Vectashield mounting medium (Vector Laboratories, H-1200-10), covered with coverslip and sealed with nail polish. For super-resolution imaging, the sections were postfixed with 4% PFA for 10 min, washed again 3 times for 10 min in 0.1 M PB and mounted onto coverslips.

Table 1. List of primary and secondary antibodies used in the study.

Antibody	Source	Identifier	Dilution
Guinea pig anti-MAGL	Frontier Institute	Cat# MGL-GP-Af200; RRID: AB_2716807	1:200
Rabbit anti-RFP	Rockland	Cat# 600-401-379; RRID: AB_2209751	1:2000
Mouse anti-RFP	Rockland	Cat# 200-301-379; RRID: AB_2611063	1:2000
Goat anti-GFP	Abcam	Cat# ab5450; RRID: AB_304897	1:2000
Guinea pig anti-GLT-1	Millipore	Cat# AB1783; RRID: AB_90949	1:1000
Rabbit anti-Glutamine Synthetase	Abcam	Cat# ab49873; RRID: AB_880241	1:10000
Rabbit anti-MAP2	Millipore	Cat# AB5622; RRID: AB_91939	1:1000
Mouse anti-Bassoon	Abcam	Cat# ab82958; RRID: AB_1860018	1:3000
Mouse anti-GFAP	Millipore	Cat# MAB3402; RRID: AB_94844	1:1000
Rabbit anti-GFAP	Millipore	Cat# AB5804; RRID: AB_2109645	1:1000
Mouse anti-NeuN	Millipore	Cat# MAB377; RRID: AB_2298772	1:500
Rabbit anti-Iba1	FUJIFILM	Cat# 019-19741; RRID: AB_839504	1:2000
Alexa 488 donkey anti-mouse	Jackson	Cat# 715-545-150; RRID: AB_2340846	1:400
Alexa 488 donkey anti-rabbit	Jackson	Cat# 711-545-152; RRID: AB_2313584	1:400
Alexa 594 donkey anti-mouse	Jackson	Cat# 715-585-150; RRID: AB_2340854	1:400
Alexa 594 donkey anti-rabbit	Jackson	Cat# 711-585-152; RRID: AB_2340621	1:400
Alexa 647 donkey anti-mouse	Jackson	Cat# 715-605-150; RRID: AB_2340862	1:400
Alexa 647 donkey anti-rabbit	Jackson	Cat# 711-605-152; RRID: AB_2492288	1:400
Alexa 647 donkey anti-goat	Jackson	Cat# 705-605-147; RRID: AB_2340437	1:400
Alexa 647 donkey anti-guinea pig	Jackson	Cat# 706-605-148; RRID: AB_2340476	1:400
CF 568 donkey anti-mouse	Biotium	Cat# 20105; RRID: AB_10853136	1:1000
CF 568 donkey anti-rabbit	Biotium	Cat# 20098; RRID: AB_10557118	1:1000

The dual-color STORM imaging experiment demonstrated that there was no antibody cross-reactivity for the MAGL antibody in our experimental settings. As a word of caution, we noted that the MAGL antibody lost its efficacy upon storage for 5–6 months and cross-reaction appeared with other primary antibodies. We observed this phenomenon multiple times and with different storage conditions. Therefore, we only used fresh, few weeks-old antibody batches in our MAGL-immunolabeling experiments.

3.8. RNAscope *in situ* hybridization

Mgll$^{+/+}$ and *Mgll*$^{-/-}$ littermate mice were deeply anesthetized by isoflurane and perfused with 4% PFA. The brains were sectioned to 50-μm-thick sections and mounted on positively charged microscopic glass slides (Fisher Scientific). The sections were dehydrated in a series of ethanol solutions (50%, 70%, 100%) and kept in 100% ethanol overnight. On the following day, the sections were dried, and a barrier was drawn around them by using a hydrophobic pen (ImmEdge Hydrophobic Barrier, Vector Laboratories).

In situ hybridization was performed based on the protocol provided by the manufacturer Advanced Cell Diagnostics (ACD). The RNAscope probes were ordered from ACD (*mgll*, Cat No.: 478831, target region: 2–1357; *glul*, Cat No.: 426231-C3, target region: 103–973).

3.9. Confocal imaging

Low-magnification large images were taken using a 20× objective (CFI Plan Apo VC Air 0.75 NA) on a Nikon A1R confocal laser-scanning microscope operated by NIS-Elements AR software 4.50.0.

3.10. Single-color and dual-color STORM image acquisition

For STORM image acquisition and analysis, we followed the workflow described in detail in our earlier protocols[24,26]. Briefly, dried sections mounted on coverslips were covered just prior to imaging in STORM imaging buffer containing thiol-based switching agent and oxygen-scavenging system (0.1 M mercaptoethylamine, 5% glucose, 1 mg/mL glucose oxidase, and 1500 U/mL catalase in Dulbecco's phosphate-buffered saline (DPBS)). For dual-color STORM imaging, the sections were mounted in Smart buffer (Abbelight). Sections were sealed with nail polish or Twinsil (Picodent), dried for 10 min, and inserted onto the microscopic stage of a Nikon N-STORM system that was equipped both with a C2 confocal scan head and an Andor iXon Ultra 897 EMCCD camera and was operated by the NIS Elements AR 4.3 software and N-STORM 3.4 module.

First, to locate the electroporated astrocytes, a low-magnification large image was taken by using a CFI S Plan Fluor 20× 0.45 NA objective. After switching to a high-magnification objective (CFI Apo TIRF 100× Oil 1.49 NA), we performed direct STORM (dSTORM) imaging. Laser powers for the different lines (647 nm, 300 mW, MPB Communications VFL-P-300-647; 405 nm, Melles Griot 56RCS/S2780; 488 nm, Coherent sapphire 488-200 CW; 561 nm, Coherent sapphire 561-100 CW), as well as switching the laser beam between total internal reflection fluorescence (TIRF) and confocal light paths were adjusted by acousto-optical tunable filters (AOTFs). The focus was stabilized with a perfect focus system (PFS). A cylindrical lens inserted into the light path enabled 3D imaging and the z-coordinates of localization points could be retrieved from calibration curves that were obtained from imaging of fluorescent beads attached to

coverslips. Before acquiring the STORM image, fluorophores were pushed to their dark state by illumination with their respective laser lines. Next, we tilted the angle of the laser beam from standard epi-illumination to near-TIRF using a TIRF illuminator (equipped also with 2× and 4× beam focusing lens) to reduce the out-of-focus fluorescence. For single-color STORM imaging, the 647 nm laser line was used with a STORM filter cube (DM: 660 nm; EM: 670–760 nm). The reactivation rate of fluorophores was adjusted by increasing the power of the 405 nm activation laser to the desired level without introducing overlapping blinking events. For dual-color STORM imaging, a QUAD-band filter cube (Chroma, 97335) was used in a sequential imaging protocol. First, the target-of-interest was imaged by using the 647 nm laser line. Next, we pushed the CF568 fluorophores to their dark state in epi-illumination by using the 561 nm laser line. Subsequently, the TIRF angle was readjusted, and a STORM image was acquired. We found this sequential imaging strategy superior compared to alternating laser lines in each frame, because the abundant astrocytic CF568 localizations required a few tens of seconds of illumination prior to imaging, a step that would quench most of the AF647 fluorophores.

Embryonic brain sections were imaged on the same N-STORM system with single-color STORM. Sections were covered with freshly prepared imaging medium containing 0.1 M mercaptoethylamine and an oxygen-scavenging system (5% (m/v) glucose, 1 mg/mL glucose oxidase and 2.5 μL/mL catalase in DPBS), sealed with nail polish and placed onto the microscope stage after 10 min. The GFP-positive radial processes of radial glial progenitor cells and the nestin-immunopositive intermediate filaments were located in the cortical plate in confocal z-stacks to determine the optical plane for subsequent STORM imaging. Continuous illumination with the 405 nm laser line was used to reactivate the fluorophores, and 2500–5000 cycles were captured using 647-nm excitation.

3.11. Correlated confocal and STORM imaging

To resolve differences in astrocytic morphological detail across imaging scales, as well as to determine the distribution of astrocytic MAGL localization points in relation to synapses labeled by Bassoon, we first acquired a confocal z-stack (size: 512 × 512 pixels, pixel size: 80 nm, z-step size: 150 nm, z-range: 2 μm) from the very same region of

interest that was subsequently imaged by the STORM microscope. Confocal images were deconvolved with Huygens software (SVI) using the CMLE algorithm.

3.12. STORM image analysis

Peak detection of individual localization events was performed by the N-STORM module that relies on the 3D-DAOSTORM algorithm. In case of the sequentially acquired dual-color images, the drift correction of the last localization detected in the first image (647-nm channel) was additionally applied for all the localizations of the second image because the software considers the two STORM movies as independent imaging sessions. The level of chromatic aberration between the 647/561 laser lines was assessed in advance on TetraSpeck beads attached onto coverslips and was found to be negligible in *xy* dimensions and ~60 nm in the *z* dimension. Therefore, the *z*-coordinates of the far-red channel were shifted by 60 nm. The localization points from both channels were then clipped from the original 800-nm axial range (±400 nm from the focal plane) to a 600-nm range (±300 nm from the focal plane), thereby avoiding non-overlapping regions in the *z* dimension. Note that localizations are detected with a Gaussian probability along the axial dimension, and therefore the relative abundance of localization points may also be slightly shifted axially to each other. Because the 2× TIRF focusing lens introduces inhomogeneity at the edges of the imaging area, we filtered for localizations detected in the center of the camera ROI (corresponding to 10,240 nm^2, 1/4 of the imaged area).

Custom written Python codes were used in conjunction with various software to analyze the STORM data. To determine the channel crosstalk in STORM images, the astrocytes labeled with a single fluorophore were sequentially imaged using their respective 647-nm and non-specific 561-nm lasers in case of immunolabeling with a far-red dye-conjugated secondary antibody and vice versa. Crosstalk was determined as the ratio of the number of non-specific/specific localization points. Images were also taken from areas where no labeled astrocytes were present. The number of localization points detected here was considered as background and was subtracted from their respective images. When different peak identification thresholds were used to retrieve the number of localization points from the non-specific illumination, the threshold for the specific illumination was kept constant.

To assess the level of colocalization of dual-labeled astrocytes, we retrieved the Manders' coefficient values from Voronoi tessellations using Coloc-Tesseler[79]. To determine whether there is a systematic bias in the localizations due to chromatic aberration, we shifted the localizations of one channel in *xy* dimensions relative to the other from −60 to 60 nm in 20 nm increments and calculated the Manders' values for all possible offset combinations. We found that the shifts decreased Manders' values, indicating the lack of *xy* chromatic aberration. Following channel shifting, non-overlapping regions were excluded from both channels to avoid biasing the colocalization analysis by introducing artificial padding. Two-dimensional Voronoi cells were generated, with the threshold value for object creation set to 1 in both channels. Although the 647-nm channel contained more localizations because AF647 exhibited superior blinking compared with CF568, Manders' coefficients reflect the degree of co-occurrence rather than the exact stoichiometric relationship between the two channels. Therefore, these values are relatively insensitive to differences in target density between channels. To assess the co-occurrence of astrocytic localization points with the protein of interest (GS, Bassoon, GLT-1, MAP2), we created 3D Voronoi cells in Coloc-Tesseler. Because many localization points on the edges of relevant structures were discarded with threshold values of 1, we set 0.5 for thresholding both channels. Notably, false colocalizations did not occur with these lower threshold settings. We used AutoHotkey scripts to automate Coloc-Tesseler for opening the images, adjusting parameters and saving the results.

To filter MAGL localization points belonging to astrocytes, we created 2D Voronoi cells from the astrocytic localization points in SR-Tesseler[80], constructed objects reflecting astrocyte processes with a threshold (density factor) = 1.5 and saved the output image. Then, we evaluated the contours of these objects on the output image using the OpenCV module in Python and determined the scaling factor between the pixelated image and the STORM image to retrieve the coordinates of the astrocytic contours in the STORM coordinate system. The Matplotlib Path module was used to test if a localization point is located inside these polygons and therefore can be assigned as a localization point representing MAGL in astrocytes. To determine if MAGL is enriched inside astrocytes, we rotated the MAGL STORM image relative to the astrocyte STORM image and compared the ratio (mean value from rotations by 90, 180, 270 degrees) of astrocytic/non-astrocytic points to the ratio obtained from the original image.

To test if astrocytic MAGL blinking events are enriched near synapses marked by Bassoon, we acquired correlated confocal and STORM images. To match the axial range of the STORM localization points, a maximum-intensity projection (MIP) was generated from the three central optical sections of the deconvolved confocal z-stacks. The two different imaging modalities were loaded in the VividSTORM software[24], the offset between them was determined, and STORM localization points were shifted with this value. Next, Otsu's algorithm was applied to the original Bassoon confocal z-stack rather than to the MIP. The resulting binary image was converted into a point-coordinate list by multiplying the voxel indices by the lateral pixel size and axial z-spacing, thereby obtaining the x, y, and z coordinates of each segmented voxel. MAGL blinking events were identified by DBSCAN (SciPy module, $n = 5$, epsilon = 100 nm). For each astrocytic MAGL blinking event (center of mass), we determined the nearest neighbor distance (NND) of the thresholded Bassoon voxels. Next, while preserving the spatial pattern of individual MAGL blinking events, we randomized their positions 100 times within their respective astrocytic contours. We then calculated the NNDs to Bassoon-positive voxels for each randomized dataset and compared the cumulative distributions of the original and randomized datasets. NNDs were calculated using the SciPy spatial module in Python.

To analyze the nanoarchitecture of radial glia processes, the confocal images and the 3D coordinates of nestin localization points were loaded and aligned in VividSTORM[24]. The number and density of localization points were calculated in randomly selected, identically sized filament segments used as regions of interest. After fitting a convex hull onto the outermost localization points, the volume and surface area of the filaments were measured. Intensity profiles perpendicular to the nestin filaments were measured, and full-width-at-half-maximum (FWHM) values were calculated by fitting a Gaussian function in the NIS-Elements software. Convex hull and 3D-rendering images were obtained with the Visual Molecular Dynamics software.

3.13. Statistical analysis and figure preparation

GraphPad Prism 9 software was used for statistical analysis and graph construction. Comparing the distribution of large datasets (nearest neighbor distances of all localization points) using Kolmogorov–Smirnov statistics was done via Python's SciPy package.

Figures were produced in Adobe Illustrator. The color and contrast of microscopic images were adjusted in Adobe Photoshop, where images were treated in the same manner for all groups or genotypes. STORM localization points with intensities reflecting localization precision were exported from NIS Elements N-STORM module after applying density filtering. The Visual Molecular Dynamics (VMD) software was used to visualize molecules as spheres. Single or dual-color tessellated images were exported from SR-Tesseler or Coloc-Tesseler, respectively. AI-based language models were used exclusively for minor linguistic rephrasing of author-written text and did not contribute to the scientific content of the thesis.

Data from the *in utero* electroporation experiments were tested with Statistica 13.1 (TIBCO) and Prism 5 (GraphPad). Normality was assessed with the Shapiro–Wilk test. For the nestin STORM measurements, values were averaged per animal and compared between the GFP and ΔnCdh2-GFP conditions with two-sided Mann–Whitney U tests (n = 3 animals per condition). The level of significance was set to $P < 0.05$.

4. Results

The results presented in this chapter were published in László et al., 2020[78] and Zöldi and Katona, 2026[77], from which parts of the text, figures and figure legends are adapted. These publications are therefore not cited repeatedly; additional findings from them that are not shown in this thesis are cited in the text.

4.1. Electroporation as a sparse labeling method for subsequent super-resolution imaging

4.1.1. Examining the architecture of radial glial cells labeled by *in utero* electroporation

Radial glial progenitor cells (RGPCs) have long been a focus of our research. RGPCs are neural stem cells that produce various cell types such as neurons, astrocytes and oligodendrocytes during brain development. They reside along the ventricular surface and undergo asymmetric cell divisions: the non-RGPC-fated daughter cells detach from the ventricular wall and migrate to their target locations using the radial scaffold provided by the self-renewed RGPCs[81]. Prematurely detached cells that still retain their proliferative capacity at ectopic locations represent a serious risk factor for brain malformations[82]. Despite the vast number of cell divisions during embryonic development and the various pathological insults that lead to untimely detachment, brain malformations are relatively rare. This led us to hypothesize the existence of a safeguarding mechanism that selectively eliminates prematurely and pathologically detached progenitor cells, while preserving the timely delaminated daughter cells.

To model premature delamination errors, we utilized an adherens junction injury protocol. N-cadherin is a key molecular component of the adherens junction belt that anchors neighboring RGPCs along the ventricular wall[83]. Introducing a dominant-negative form of N-cadherin (ΔnCdh2-GFP) into the lateral ventricles by *in utero* electroporation at embryonic day 14.5 (E14.5) caused the destruction of adherens junctions at the electroporated area 24 hours after the perturbation (Fig. 3a-f, work of co-authors of ref. [78]). As a result, RGPCs delaminated from the ventricular surface and accumulated in the subventricular zone (SVZ) 48 hours later. Importantly, despite being

outside of the ventricular zone, RGPCs still retained their identity and proliferative capacity[78].

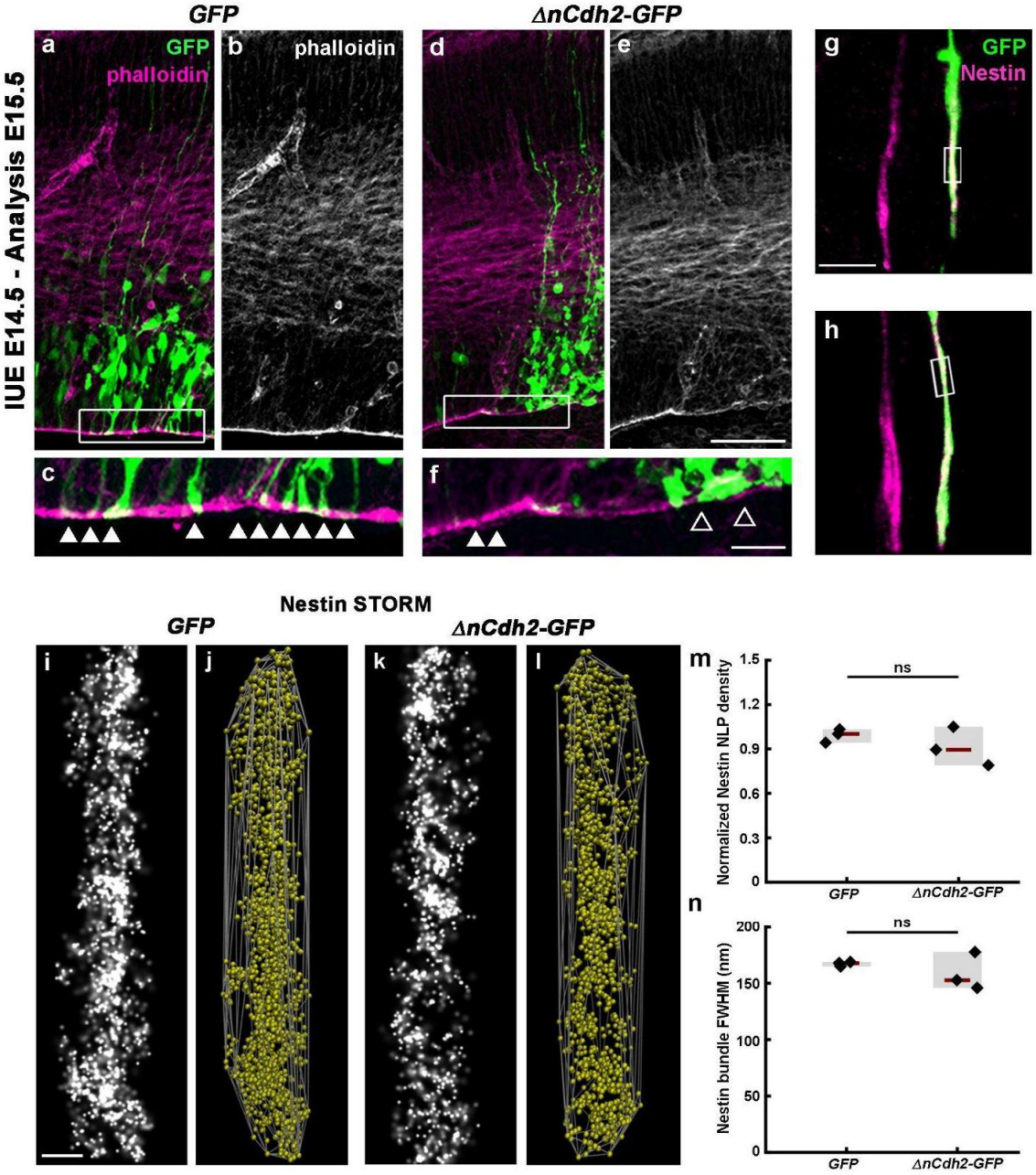


Figure 3. STORM imaging following in utero electroporation reveals unaltered radial glia scaffold in an adherens junction perturbation model. *(a-f) Electroporating ΔnCdh2-GFP, but not the control GFP, specifically dismantles the adherens junction belt around the affected apical endfeet of RGPCs. The adherens belt is visualized by the high-affinity F-actin probe phalloidin coupled to Alexa Fluor 568. Panels a-f show the work of co-authors of ref. [78]. (g-l) Correlated confocal and STORM super-resolution imaging*

of the radial glia scaffold labeled by nestin shows intact glial processes. STORM data on panels (i-j) and (k-l) are from the boxed region in (g) and (h), respectively. (j, l) are convex hull representations of the corresponding STORM images. (m-n) Neither the density of nestin localization points (NLP), nor the FWHM values of nestin filament bundles were different in the perturbed model compared to the control (two-sided Mann-Whitney U test, ns = not significant, P = 0.7 and P = 0.55 in panels (m) and (n), respectively; n = 3 animals in all cases. Median is shown as a red line). Scale bars: (a-f): 50 μm; (g-h): 5 μm; (i-l): 200 nm.

The adherens junction disruption exhibited a striking specificity – it was not only restricted to the electroporated area, but the basal processes of the labeled RGPCs still reached the pial surface and seemed to be intact[78]. To test whether the radial glia scaffold indeed remained unaltered, we immunolabeled the samples for nestin, an intermediate filament abundant in RGPC processes. We carried out STORM super-resolution imaging of nestin and correlated the molecular information with its respective confocal signal (Fig. 3g-l). This enabled us to restrict the analysis to only those cells that were labeled by electroporation. The density of nestin STORM localization points (LP) was similar in the perturbed (ΔnCdh2-GFP) and control (GFP) RGPCs, suggesting an identical scaffold architecture (Fig. 3m). In line with this, the width of nestin bundles (as quantified by the full width at half maximum, FWHM, of STORM LPs) also remained unaltered (Fig. 3n). Of note, FWHM values were around 150 nm, below the diffraction limit of conventional light microscopy, where subtle changes may remain hidden. These findings allowed us to confirm that the detachment is triggered by the disrupted adherens junctions accompanied by the loss of N-cadherin signaling, rather than by changes in the radial glial cell architecture.

Besides premature detachment of RGPCs, adherens junction disruption also resulted in an increased cell death as visualized by TUNEL labeling[78]. Importantly, we identified abhydrolase domain containing 4 (ABHD4), an endocannabinoid-metabolizing enzyme with a yet unknown *in vivo* function as a necessary and sufficient molecular player that mediates this caspase-dependent cell death. Anoikis is a specific form of apoptosis induced by the loss of anchorage in epithelial cells and is considered a protective mechanism in tumor biology. Due to its conceptual similarity, we termed this process developmental anoikis, a safeguarding mechanism that eliminates the

prematurely delaminated cells during brain development. Importantly, we found that teratogenic insults such as maternal alcohol exposure can also activate this pathway[78].

The above detailed experiments revealed that electroporation can be successfully utilized as a labeling method that identifies cells of interest for correlative confocal and STORM super-resolution imaging. Electroporation achieves a sparse labeling, which can be beneficial when investigating the effects of various perturbation models where global, systems-level approaches may result in unwanted compensatory mechanisms. Specificity is enabled by the timing of electroporation to select the appropriate pools of neural stem cells. Importantly, these stem cells then develop into neurons and astrocytes, expanding the applicability of the method to other cell types.

4.1.2. STORM imaging reveals the nanoscale morphology of hippocampal astrocytes labeled by postnatal electroporation

Neurogenesis and gliogenesis follow a sequential pattern: radial glial cells produce neurons first, followed by astrocytes later in early brain development[81]. Indeed, while the radial glia we labeled at E14 will develop into neurons[78], delaying the timing of electroporation to E18 or later will result in the labeling of astrocytes[84]. These later timepoints, however, are much closer to pup delivery, and cause unnecessary stress to the dams. Interestingly, astrocytes are still being generated from radial glia cells at birth and early neonatal ages, making it possible to carry out electroporation on the newborn pups. This technique, called postnatal astrocyte labeling by electroporation (PALE)[53,85,86] spares the dams from surgery, and therefore is much easier to adopt than its *in utero* form.

To the best of our knowledge, however, PALE has only been used to label neocortical astrocytes[87], restricting its use in neuroscience research. We hypothesized that simply by adjusting the position of the electrode[88], we could target hippocampal astrocytes as well. This would be of primary interest, as many of the astrocytic physiological observations (especially the endocannabinoid and MAGL-related ones[61–63]) come from the hippocampus. Therefore, we injected a plasmid encoding Green Fluorescent Protein fused to Channelrhodopsin-2 (ChR2-GFP) into the lateral ventricles of newborn (postnatal age 0 to 1 day, P0-P1) pups and carried out electroporation in a way that would target hippocampal astrocytes (Fig. 4A). Investigating the distribution of GFP^+ cells in adult mice revealed sparsely labeled hippocampal astrocytes in the stratum

radiatum, pyramidale and oriens of CA1 (Fig. 4B-D). All the GFP^+ cells showed the characteristic spongiform morphology of astrocytes and expressed the astrocytic marker glial fibrillary acidic protein (GFAP) and glutamine synthetase (GS) (Fig. 4E, F), but not the neuronal marker NeuN or microglial marker Iba1 (Fig 4G, H).

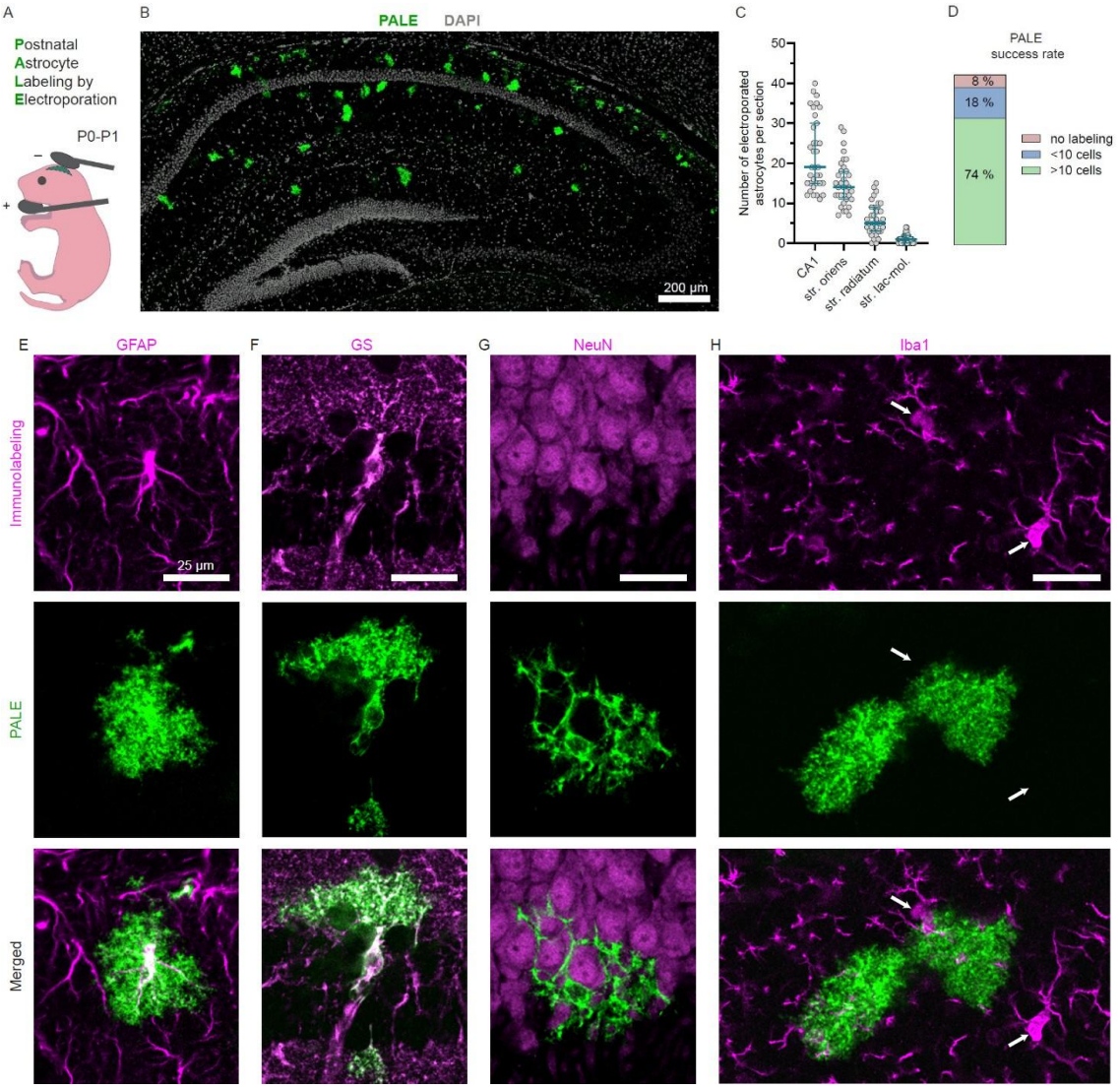


Figure 4: Postnatal Astrocyte Labeling by Electroporation (PALE) demarcates complex astrocytic arbor topography within dense brain tissue. *(A) Schematics of the PALE (Postnatal Astrocyte Labeling by Electroporation) method. (B) Confocal image shows that PALE enables sparse and specific labeling of hippocampal astrocytes. (C) Quantification of the labeled cells across the CA1 hippocampal layers. (D) Reproducibility of the method. (E-H) Specificity of the PALE method. The electroporated*

astrocytes express the astrocytic markers glial fibrillary acidic protein (GFAP) (E) and glutamine synthetase (GS) (F), but not the neuronal or microglial markers NeuN (G) or Iba1 (H), respectively. For the above markers n = 58, 45, 29, and 42 cells were analyzed, respectively. Arrows in (H) highlight microglial cell bodies adjacent to labeled astrocytes.

GFAP is still widely used to measure alterations in astrocytic architecture. However, GFAP as an intermediate filament labels only the widest branches of the astrocytic arbor[89]. By contrast, the electroporated fluorescent proteins visualize the full extent of astrocyte morphology (Fig. 4E). Of note, only plasma membrane-targeted, but not cytosolic, fluorescent probes can reconstruct the finest astrocytic processes due to their high surface to volume ratio[90]. Moreover, while electroporation delivers the probes to the labeled cells at high density enabling full morphological reconstruction, the sparse cell labeling ensures low fluorescent background above and below the focal plane, a prerequisite for high-quality STORM imaging in tissue. It is important to note that the routinely available mouse lines to date provide only high labeling density of astrocytes and/or express cytosolic fluorescent probes[91].

High-magnification confocal images showed the well-known intricate morphology of the astrocytic arbor (Fig. 5A), with many processes merging together and indistinguishable from each other at the resolution of confocal microscopy even after deconvolving the images. We immunolabeled the membrane-targeted GFP using primary and secondary antibodies, the latter carrying Alexa Fluor 647 (AF647) fluorophores. STORM images from the very same field of view revealed a much sharper and more detailed view of the astrocytic arbor (Fig. 5B). We also observed loop-like structures as described recently using STED microscopy[50,51] that appeared as genuine, continuous loops in confocal z-stack images (Fig. 5C). The improved resolution of STORM, however, could reveal that some of these loops were non-continuous[51,52], and only astrocytic segments crossing each other along the axial dimension created the false impression (Fig. 5D). Intensity measurements showed that the distance at which the intensity of a segment drops from maximal to background levels is also much narrower when using STORM (Fig. 5E-G). This may result in false assessment of co-localization when imaging closely located non-astrocytic proteins using classical light microscopic methods.

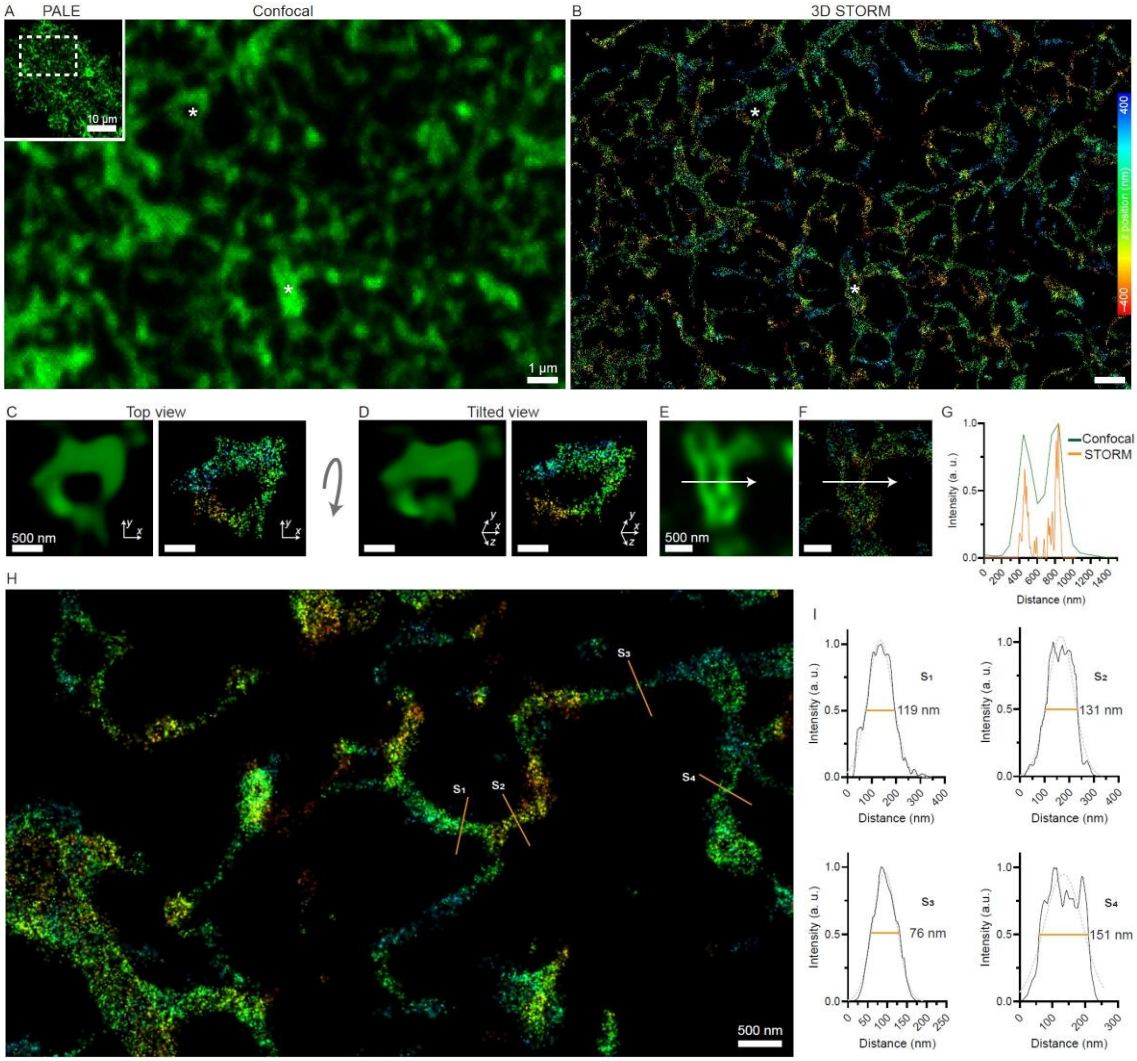


Figure 5: 3D-STORM super-resolution imaging readily outlines ultrathin astrocytic processes beyond diffraction-limit. *(A) High magnification confocal image of a single electroporated astrocyte. Stars denote features that are shown on subsequent figure panels. (B) 3D STORM super-resolution image of the very same field of view. Color coding is based on the axial depth of localization points relative to the focal plane. Stars denote features that are shown on subsequent figure panels. (C) Enlarged view of a loop-like structure from panel (A) and (B). The confocal image was deconvolved and 3D reconstructed from 3 planes, corresponding to the range of STORM imaging. (D) Tilted view of the very same structure as in (C). STORM reveals that this loop is only partial and non-continuous along the z direction. (E-G) Intensity measurement along the same structure from corresponding confocal and STORM image pairs, labeled by stars in A*

and B. (H) STORM imaging of another PALE-labeled astrocyte, but electroporated with an alternative membrane-targeted tag, Lck-GFP. The fine morphological details are similar to the ChR2-GFP-porated astrocytes. (I) Intensity measurements along some astrocytic segments ('S', orange lines in H). Process width is determined from the full width at half maximal (FWHM) values.

The overexpression of ChR2, which was used only to deliver GFP to the plasma membrane but not to perform optogenetics, may alter the physiology and hence the morphology of the cells. Therefore, we electroporated astrocytes with an alternative membrane-targeting construct, Lck-GFP[90]. STORM imaging of astrocytes labeled with Lck-GFP showed similar nanoscale anatomical features (Fig. 5H). The spongiform astrocytic domains showed narrower and wider sections alternating on the very same segments, which may correspond to the shafts and nodes or to the analogous constrictions and expansions, described via STED[50] and electron microscopy[92], respectively. Intensity measurements along some narrower sections showed that their widths as quantified by the full width at half maximal values are well below the diffraction limit, and hence confocal microscopy falsely enlarges these structures (Fig. 5I). In conclusion, the above findings demonstrate that STORM imaging of astrocytes labeled by PALE is a robust method to reveal the astrocytic nanoarchitecture in intact brain tissue.

4.2. Dual-color STORM imaging of hippocampal astrocytes in brain tissue

4.2.1. Microscopic control measurements for dual-color STORM imaging

Investigating nanoscale protein distributions in biological structures that are beyond the diffraction limit requires multi-color STORM imaging. When introducing a second STORM channel, one has to ensure that the imaging scheme is free of crosstalk and microscopic aberrations to enable unambiguous data interpretation. This needs to be done on each microscopic setup, as subtle differences such as the power of the excitation or activation laser, the type of dichroic mirror, imaging depth, or identification settings for single-molecule events can all have an impact on the imaging quality.

First, we aimed to reconstruct the astrocytic arbor by using a spectrally distinct fluorophore, CF568. When exciting CF568 with its respective high-power laser line, the abundant PALE-GFP signal was also excited, elevating the fluorescent background to a

level where the blinking of CF568 fluorophores was hardly discernible. Thus, we switched to ChR2-mCherry as a PALE marker, which was bright enough to validate the success of electroporation without any intensification, but could be easily bleached during STORM imaging, allowing the accurate reconstruction of astrocytes when labeling mCherry by anti-mCherry antibodies coupled to CF568 (Fig. 6A).

To evaluate the degree of channel crosstalk, we imaged the same astrocyte with its non-specific laser line (647 nm, i.e., the laser line for the other STORM channel). Only a few unstructured localization points could be detected, whose number just slightly depended on peak identification stringency (Fig. 6B, C). However, this was not the case the other way around (Fig. 6D). When exciting an AF647-labeled astrocyte with its non-specific laser line (561 nm), the astrocytic labeling appeared as a structured low-intensity fluorescent background, and false localization points were identified with the peak identification settings we generally use, producing crosstalk as high as 40%. Simply increasing the stringency for peak identification, however, fully eliminated these artificial localizations (Fig. 6E, F), while the CF568-labeled astrocytes could still be reconstructed with the desirable quality.

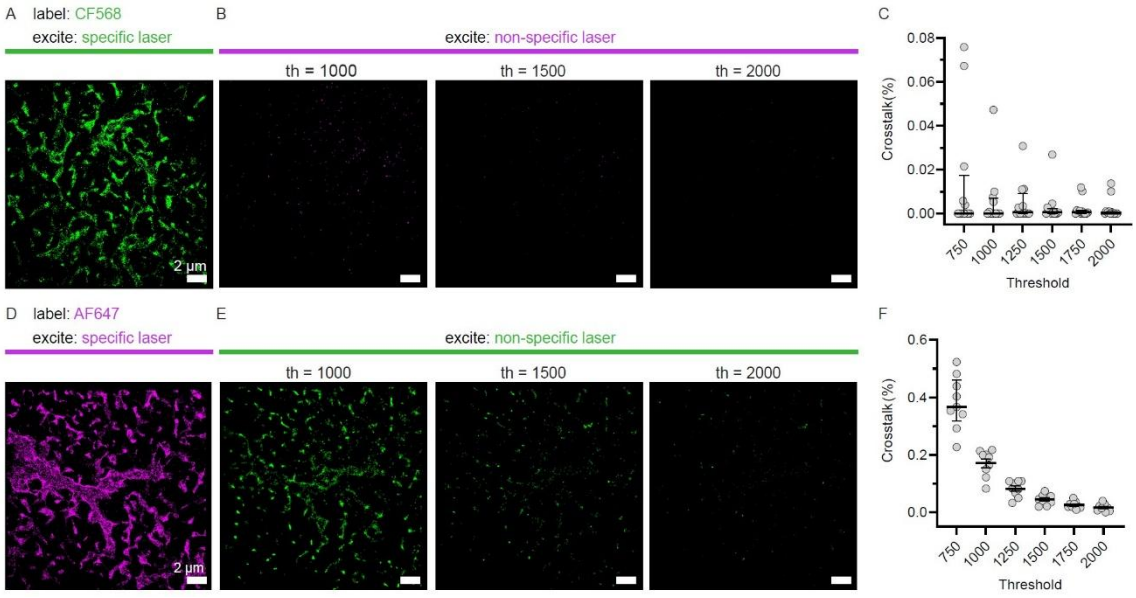


Figure 6: Adjusting peak identification thresholds carefully enables crosstalk-free multicolor STORM imaging. *(A) STORM super-resolution image of an astrocyte labeled with the CF568 fluorophore and excited with its respective (561 nm) laser line. (B) Exciting the very same astrocyte with the other, non-specific laser line (647 nm) only*

results in a few, unstructured localization points, whose number only minimally decreases with more stringent identification parameters ("th" refers to threshold for peak identification). (C) Quantification of crosstalk at different threshold parameters for the non-specific laser line. Crosstalk was determined from localization point number ratios obtained from imaging the very same astrocyte with its specific and non-specific laser line. Background localization point numbers (obtained from areas where no labeled astrocyte was located) were subtracted from the actual localization point numbers. Data are from 12 images, and are presented as median + IQR. (D-F) Same as (A-C), but with the astrocyte labeled with AF647 fluorophore, and hence the naming of the specific (647 nm) and non-specific (561 nm) laser lines is changed accordingly. (D) AF647-labeled astrocytes show superior image quality compared to the CF568-labeled ones. (E) At lower threshold settings, there is a substantial crosstalk when exciting the AF647-labeled astrocyte with its non-specific laser line. This crosstalk can be greatly reduced by elevating the thresholding stringency. (F) Summary graph of the crosstalk at different thresholding parameters for the AF647-labeled astrocyte excited with the 561 nm laser line. Data are from 9 images, and are presented as median + IQR.

Next, we aimed to determine the level of chromatic aberration, i.e., the misalignment between channels imaged with lasers of separate colors. Though imaging of fluorescent TetraSpeck beads attached to coverslips showed negligible chromatic aberration on our setup, this may not hold true deeper in tissue. Therefore, we labeled the very same astrocytes with two different secondary antibodies, carrying either CF568 or AF647 fluorophores (Fig. 7A-C). To quantify the degree of overlap we used Coloc-Tesseler[79,80] that relies on the Voronoi tessellation method to compute the popular Manders' coefficient value (a measure of co-localization) directly from the molecular coordinates and their local densities (Fig. 7D-G). Individual dual-labeled astrocytes showed a very high degree of overlap and shifting one STORM channel relative to the other by 20 nm increments in *xy* dimensions started to deteriorate the Manders' values (Fig. 7H, I). The highest Manders' values appearing at an *xy* shift of (0, 0) nm indicates that *xy* chromatic aberration, if any, is comparable in magnitude to the localization precision at imaging depths of a few micrometers. Therefore, the above data show that our microscopic setup does not suffer from severe aberrations that could compromise the true identification of astrocytic proteins inside astrocytic processes.

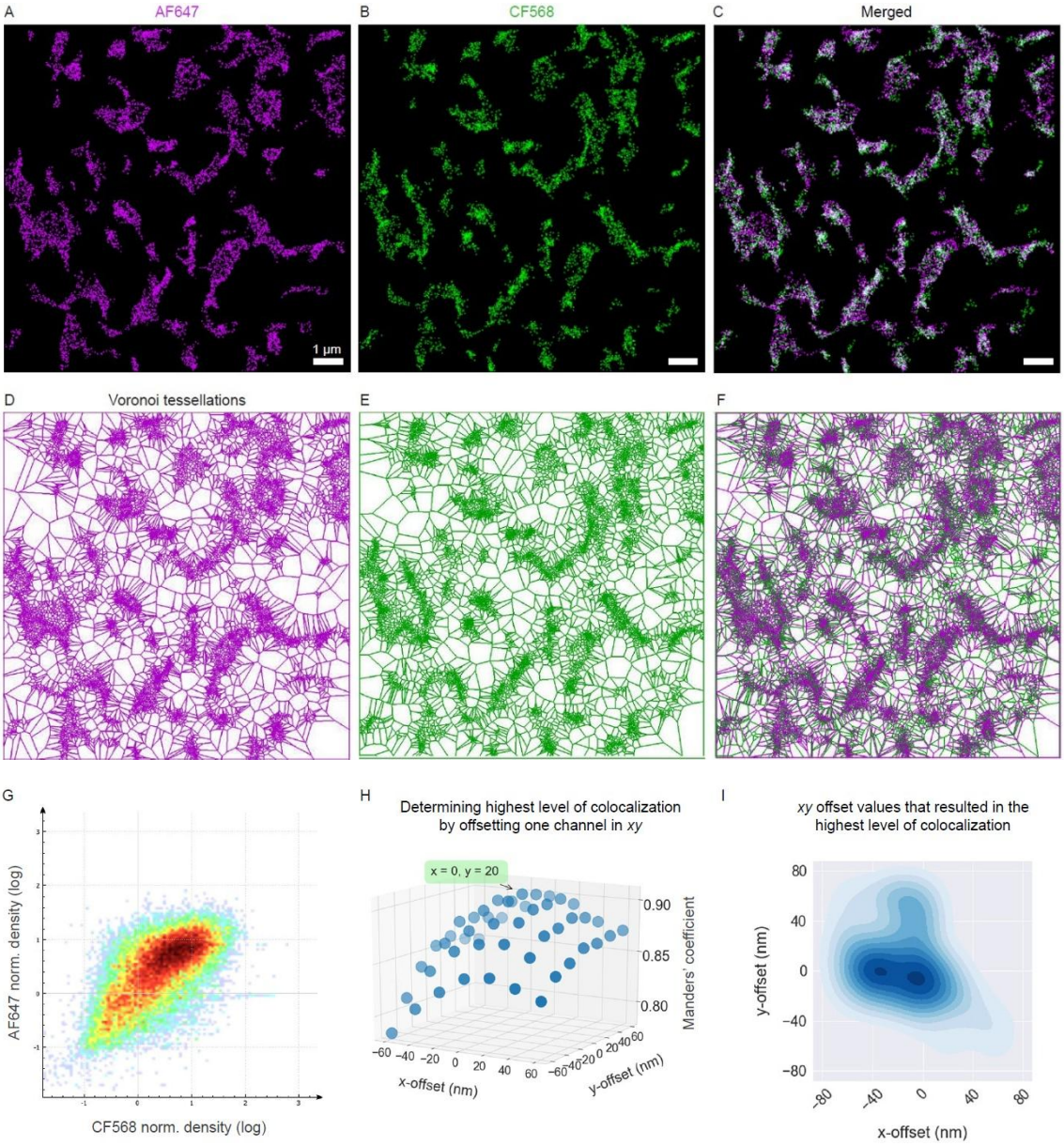


Figure 7: Chromatic aberration-free imaging, analysis and visualization of astrocytic processes in brain tissue by dual-color STORM imaging. *(A-C) Dual-color STORM super-resolution image of an astrocyte labeled both with CF568 and AF647 fluorophores, and imaged sequentially, starting with the longer wavelength laser line. (D-F) Voronoi tessellation representation of the STORM localization points for the two images. Tessellation, image creation, calculation of local densities and Manders' values were all performed in Coloc-Tesseler*[79]*. (G) The local molecular densities of the two STORM channels are highly correlated. The Manders' coefficient value that quantifies the level of co-localization can be retrieved from these pair density scatterplots*[79]*. (H) The AF647*

localization points were shifted in xy dimensions (-60 to 60 nm, 20 nm increments, independently for x and y directions) relative to the CF568 ones, and Manders' values were retrieved again. The highest values for this image were detected around 0-20 nm xy shifts, and Manders' values started to deteriorate at higher offsets. These data indicate that there is negligible chromatic aberration (and residual drift) between the imaged channels. (I) 2D histogram of the best three Manders' values retrieved from 19 images where one channel was shifted relative to the other using the above parameters. The most frequent value for both the x and y offsets is 0 nm, meaning that the two channels of the images co-localize with each other the best at their original positions.

4.2.2. Molecular imaging in sub-diffraction-limit astrocytic processes

To challenge the resolution of dual-color STORM imaging on more realistic biological examples, we visualized two targets at the nanoscale level alongside the astrocytic arbor: glutamine synthetase (GS), a cytosolic protein specific to astrocytes[93]; and Bassoon, a presynaptic active zone scaffold protein located in neuronal axon terminals[17]. If our resolution is sufficient, only the former should colocalize with the astrocytic processes, but not the latter, although many astrocytic segments, the so-called PAPs closely approach synapses – for example, half of the glutamatergic synapses in the striatum are located closer than 50 nm to astrocytic processes[94].

Dual-color STORM images revealed that GS localization points largely overlapped with the PALE localization points (Fig. 8A-D). We quantified the level of co-localization (more precisely co-occurrence) by retrieving the Manders' coefficient values from the Voronoi tessellated images[79]. As a control, the localization points of the target protein were rotated by 90 degrees. This manipulation caused the initially high Manders' values to drop to nearly 0, providing evidence that the observed co-localization values in the original image are not coincidental and cannot be attributed solely to high molecular densities (Fig. 8E). The distance between each GS localization point and its nearest neighboring PALE localization point (nearest neighbor distance, NND) was also calculated. Comparing the cumulative distribution function of the original images to their rotated counterparts reveals a strong leftward skew, indicating a dominance of small NND values (Fig. 8F). As astrocytes tile the brain by forming non-overlapping territories with very limited interdigitation[89], the vast majority of GS localizations from a domain of a

labeled astrocyte belongs solely to that individual cell, excluding the possibility that many GS localizations would fall outside of the PALE-labeled astrocyte, belonging to another non-labeled astroglial cell.

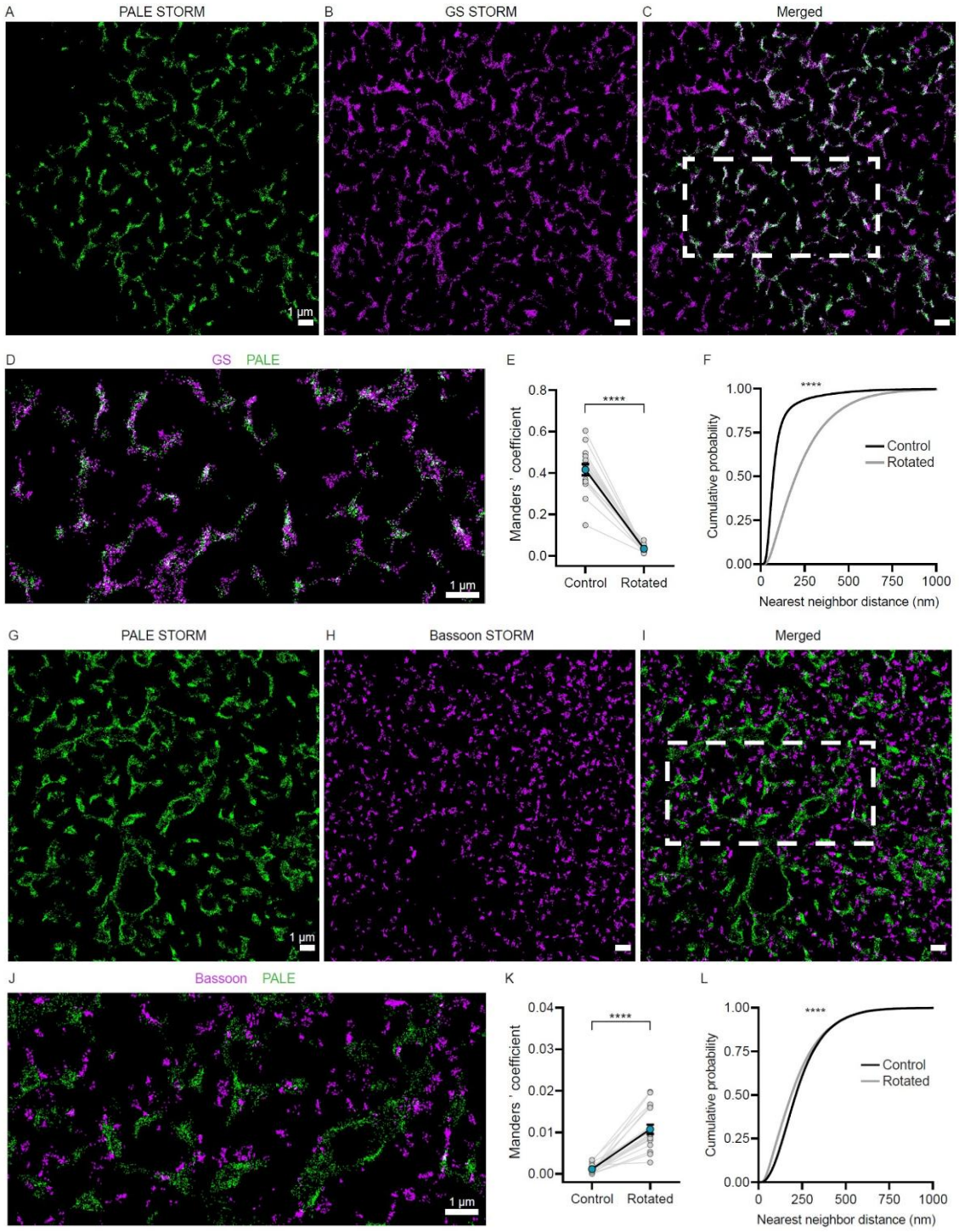


Figure 8: Cell- and compartment-specific nanoscale molecular quantification within ultrathin astrocytic processes. *(A-C) Dual-color STORM imaging of the astrocytic*

*nanoanatomy labeled by PALE and the cytosolic glial marker protein glutamine synthetase (GS). (D) Enlarged view of the box in (C) shows a complete overlap between the PALE and GS signal. (E) Manders' coefficient values (obtained from the tessellated super-resolved images) show the degree of co-localization between the original dual-color STORM images, but not between their rotated counterparts (n=16 images from 3 animals, paired t-test, ****p < 0.0001. Mean is shown in cyan with errors as ± SEM). (F) Cumulative distribution function of the nearest neighbor distances between GS and PALE STORM localization points. The distribution for the rotated control image is highly different (n=266643 localization points from 19 images from 3 animals, two-sample Kolmogorov–Smirnov test, d=0.28, ****p<0.0001. Median NND values are 71 nm for the original and 200 nm for the rotated images). (G-I) Dual-color STORM imaging of the presynaptic active zone protein Bassoon along with the astrocyte. (J) Enlarged view of the box in (I) shows a clear separation between the PALE and Bassoon localization points. (K) Manders' coefficient values indicate zero co-localization between Bassoon and the porated astrocyte. Minimal yet significantly higher Manders' values are observed in the case of rotated controls (n=20 images from 3 animals, Wilcoxon signed-rank test, ****p < 0.0001. Mean is shown in cyan with errors as ± SEM). (L) NNDs between the Bassoon and PALE localization points show very similar distributions both in the case of the original and rotated image pairs. However, there is a higher occurrence of low NND values on the rotated image (n=170089 localization points from 23 images from 3 animals, two-sample Kolmogorov–Smirnov test, d=0.05, ****p<0.0001. Median NND values are 214 nm for the original and 188 nm for the rotated images).*

STORM imaging of Bassoon (Fig 8G-J) showed a characteristic clustered pattern indicating active zones[17,25], that were often adjacent to perisynaptic astrocytic processes but still well separated without any apparent co-localization, having even lower Manders' values than their rotated image pairs (Fig. 8K). Likewise, the distribution curve of NNDs was similar between the original and rotated images, having lower NND values in the latter even more frequently (Fig. 8L). This opposite behavior of the co-localization and NND values between astrocytic and non-astrocytic targets could therefore serve as an analysis pipeline to test if a given molecule is associated with astrocytes. To confirm this, we imaged another pair of target proteins, the glial glutamate transporter GLT-1[95] and the neuronal microtubule-associated protein MAP2, and observed similar behavior of spatial

analysis data[77]. In sum, the above data show that dual-color STORM imaging has the resolution and power to reliably discriminate between astrocytic and synaptic targets in brain tissue samples.

4.3. Examining the nanoscale distribution of MAGL in astrocytes

4.3.1. Demonstrating the expression of MAGL in CA1 hippocampal astrocytes

Given the resolution of our approach, which is capable of discriminating synaptic and astrocytic proteins, we aimed to exploit its strength by visualizing MAGL selectively in hippocampal CA1 astrocytes. Notably, while *in situ* hybridization[72] and RNAscope techniques[77] revealed the mRNA expression of MAGL in CA1 astrocytes, electron microscopic studies from this brain region were able to locate this enzyme only at synaptic terminals[74,75], likely due to the inferior sensitivity of the technique.

Therefore, we carried out PALE on MAGL wild type (WT) and MAGL knockout (KO) pups. Staining for MAGL on adult hippocampal sections showed the known labeling pattern with astrocytes easily discernible in the molecular layer of the dentate gyrus[72]. The immunostaining in the hippocampus at low magnification showed a rather homogeneous pattern, with only fainter cells resembling astrocytes (Fig. 9A). All labeling disappeared in the knockout sections, confirming the specificity of the antibody (Fig. 9B). As a more direct quantification, STORM imaging in the hippocampal neuropil demonstrated much higher localization point densities for MAGL in WT compared to KO sections (Fig. 9C).

Next, we performed dual-color STORM imaging of MAGL and astrocytes labeled by PALE. As a first impression, the density of detected MAGL localization points was much higher in areas devoid of astrocytic processes, consistent with its neuronal rather than astrocytic expression (Fig. 9D). As MAGL antibodies have been reported to cross-react with other primary antibodies[72], we also took images from MAGL KO sections. Only some scattered unstructured pattern was seen in the knockout sections (Fig. 9E), ruling out the possibility of antibody cross-reactivity. We then quantified the NNDs of MAGL and PALE localization points (Fig. 9F). The cumulative distribution curve from WT sections did not show a leftward skew as would have been expected for a strong

astrocytic enrichment. However, smaller NND values were still more prominent compared to their rotated control images or to images from KO sections, indicating that a small number of MAGL localizations may be preferentially located in astrocytes.

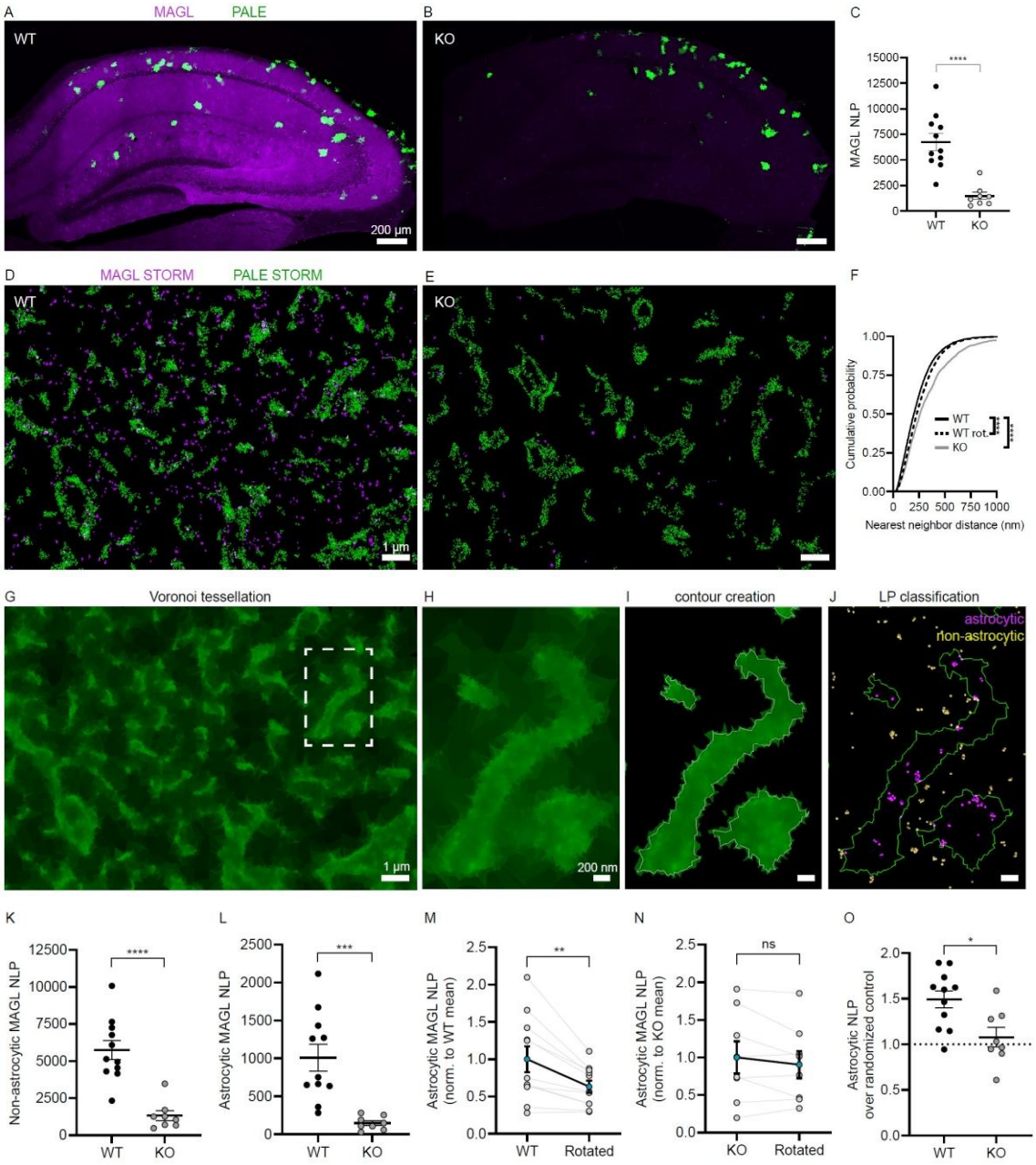


Figure 9: PALE-based segmentation and STORM-based single-molecule detection sensitivity reveals higher and lower MAGL localization-point densities in non-astrocytic and astrocytic compartments, respectively*. (A, B) MAGL labeling in MAGL WT and MAGL KO mice with astrocytes labeled by PALE. (C) Quantification of the number of localization points (NLP) in MAGL STORM images (MAGL WT n=11 images*

*from 3 animals, MAGL KO n=8 images from 3 animals, presented as mean ± SEM, unpaired t-test, ****p<0.0001). (D, E) Dual-color STORM image of MAGL and the astrocytic arbor obtained from MAGL WT and MAGL KO sections. (F) Distribution of nearest neighbor distances of MAGL and PALE localization points in MAGL WT and KO sections, and in rotated controls of the WT images (WT n=17994 localization points from 11 images from 3 animals, KO n= 2578 localization points from 8 images from 3 animals. WT vs. KO, two-sample Kolmogorov–Smirnov test, d=0.18, ****p<0.0001; WT vs. WT rotated, two-sample Kolmogorov–Smirnov test, d=0.08, ****p<0.0001). (G) Voronoi tessellation of PALE STORM from the very same area as in (E). Tessellation and image creation were performed via SR-Tesseler[80]. (H) Enlarged view of the boxed area in (G). (I) Object creation from Voronoi cells after setting a density factor. The contour of the object will serve as a region of interest (ROI) for subsequent molecule filtering. (J) MAGL STORM localization points are classified as astrocytic and non-astrocytic ones based on their positioning respective to the astrocytic contours. Localizations were visualized by the Visual Molecular Dynamics (VMD) software. (K-L) Summary graphs of MAGL STORM localization point numbers between MAGL WT and KO animals for non-astrocytic (K) and astrocytic (L) localizations (n=11 images from WT from 3 animals, and n=8 images from KO from 3 animals, presented as mean ± SEM, unpaired t-test, non-astrocytic: ****p<0.0001, astrocytic: ***p<0.001). (M-O) Summary graphs comparing the astrocytic MAGL NLPs in WT and KO sections between the original and their rotated control image pairs (WT vs. rotated, n=11 images from 3 animals, paired t-test, **p=0.0034; KO vs. rotated, n=8 images from 3 animals, paired t-test, p=0.2082; fold change over rotated controls, n=11 images from 3 WT animals, and n=8 images from 3 KO animals, unpaired t-test, *p=0.01. All data are presented as mean ± SEM).*

To determine what proportion of the MAGL localization points can be attributed specifically to astrocytes we again took advantage of the Voronoi tessellation method[80,96]. By tessellating the PALE STORM signal (Fig. 9G, H) and by setting a density threshold we created objects with contours delineating the astrocytic arbor (Fig. 9I). These contours then served us as regions of interest (ROIs) to classify MAGL localizations as either astrocytic or non-astrocytic (possibly synaptic) ones (Fig. 9J). Interestingly, we found that the densities of both non-astrocytic and astrocytic MAGL localization points were much

higher in WT compared to KO sections (Fig. 9K, L). Notably, astrocytic localization points in a given neuropil area accounted for only 14% of all localizations.

To rule out the possibility that non-astrocytic MAGL localizations were misidentified as astrocytic ones, we compared the astrocytic MAGL density in the original images to their rotated image pairs. Despite the abundant non-astrocytic MAGL localizations, however, astrocytic MAGL density was still higher than after image rotation (Fig. 9M). These data indicate that MAGL localizations, although sparse, are still enriched in astrocytes compared to the neighboring neuropil. Notably, the density of astrocytic MAGL points in KO sections was similar to their rotated control images, arguing against antibody cross-reactivity or the presence of a structured background (Fig. 9N, O).

4.3.2. The distribution of MAGL in hippocampal astrocytes suggests a synapse-independent role

Cell type-specific MAGL knockout experiments postulated different physiological roles for MAGL located either in neurons or astrocytes[62]. However, it remains elusive how the cell type-specific functional versatility of this enzyme is achieved at the molecular level, and whether nanoscale anatomical observations can predict physiological functions.

STORM images of MAGL in the hippocampal neuropil showed a distinctive clustered pattern. Indeed, when computing the Ripley's *H* function of MAGL STORM images we found that *H*(r) values had a prominent peak around 60 nm, indicating a clustering at this spatial scale (Fig. 10A). Notably, this value is much smaller than the ~225 nm for the active zone marker Bassoon imaged with identical parameters. As for STORM imaging we used secondary antibodies that carry 4-5 fluorophores, and STORM relies on photoswitchable fluorophores that can be detected multiple times, localization point clusters may be created even from single protein targets[97,98]. Indeed, randomizing localization point clusters with daughter localizations scattered around the parent localization with a standard deviation matching our localization precision (known as the Neyman-Scott process)[99] also showed a peak around 60 nm on the Ripley's *H* curve. Therefore, it is likely that the clustering we see in the MAGL data does not arise from true molecular clusters but from multiple blinking events that occur in STORM imaging. We will refer to these clustered localization points as "blinking events" to avoid any

misinterpretation. The spatial characteristics of MAGL blinking events, however, may differ inside and outside of the astrocytic processes. To address this, we first identified individual blinking events by the DBSCAN[100] clustering algorithm. Despite the lower overall MAGL densities in astrocytes, however, neither the number of localization points in individual blinking events (Fig. 10B), nor their diameter (Fig. 10C) were different compared to the non-astrocytic ones.

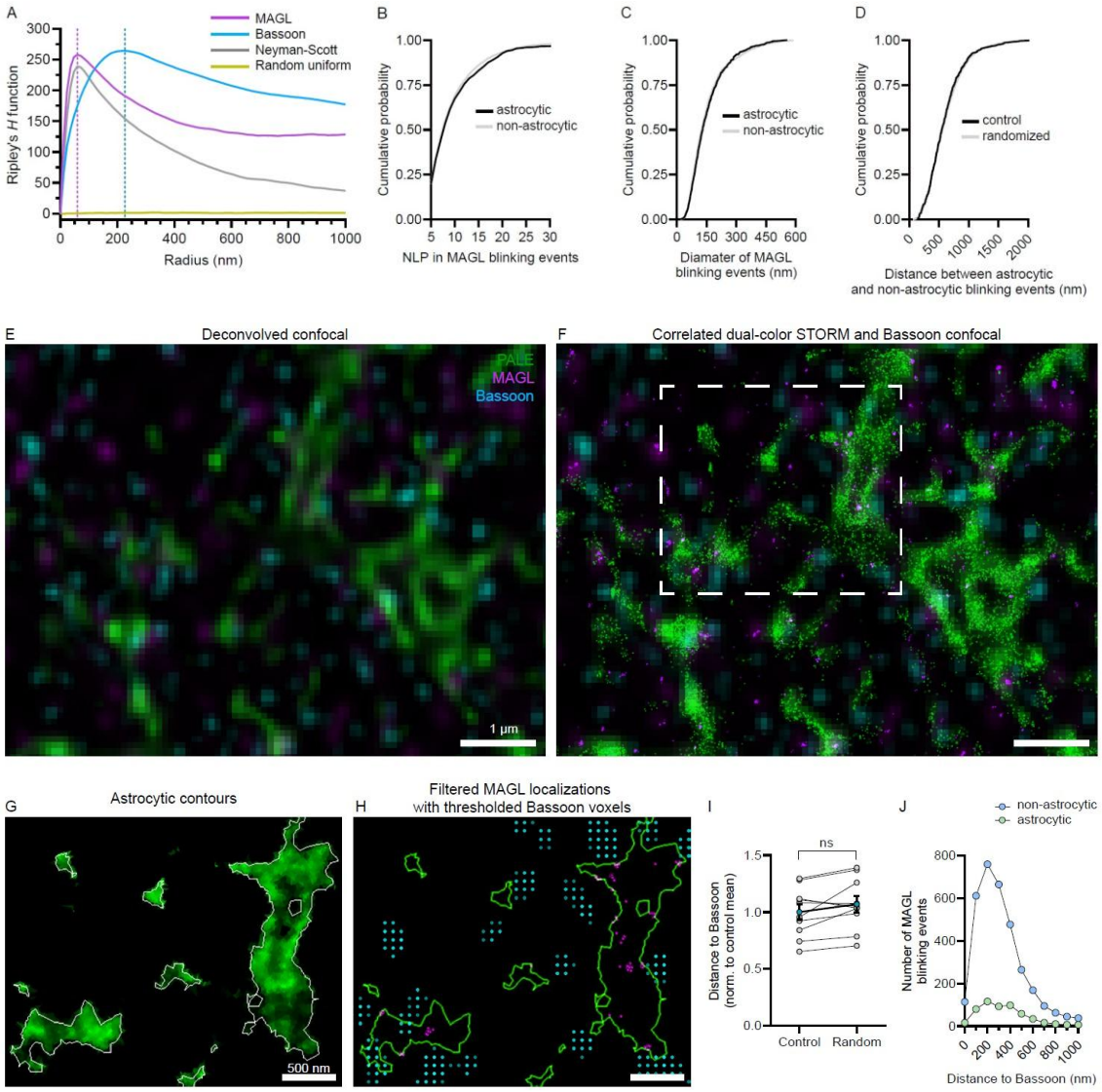


Figure 10: Tripartite synapse-independent nanoscale MAGL localizations are randomly distributed in ultrathin astrocytic processes. *(A) Ripley's H function of MAGL and Bassoon. MAGL shows a clustered distribution compared to its randomized control, with a prominent peak around 60 nm, that is much lower than the ~225 nm of the active zone marker protein Bassoon. However, simulated point clusters (Neyman-Scott process)*

also have similar spatial characteristics, suggesting that these point clusters arise from multiple blinking during STORM imaging. We will refer to them as "blinking events" in the following. (B) Astrocytic and non-astrocytic MAGL blinking events are composed of a similar number of localization points (astrocytic n=715 and non-astrocytic n=4159 blinking events from 10 images from 3 animals, two-sample Kolmogorov–Smirnov test, d=0.03, p=0.58). Blinking events were identified by the DBSCAN clustering method. (C) Astrocytic and non-astrocytic MAGL blinking events have similar diameters as determined by the maximal xy distance between localization points belonging to the same blinking event (astrocytic n=715 and non-astrocytic n=4159, two-sample Kolmogorov–Smirnov test, d=0.04, p=0.38). (D) The nearest intercluster distance between astrocytic and non-astrocytic MAGL blinking events shows a similar distribution to its randomized control, where astrocytic blinking events were randomized in their respective ROIs (astrocytic n=507 and non-astrocytic n=4823 blinking events from 11 images from 3 animals, two-sample Kolmogorov–Smirnov test, d=0.03, p=0.71). (E) High-resolution deconvolved confocal image of a PALE-labeled astrocyte, MAGL, and the active zone marker Bassoon. (F) STORM super-resolution image of the labeled astrocyte and MAGL from the corresponding field of view superimposed onto the Bassoon confocal image. (G) Identification of astrocytic MAGL blinking events (only their center of masses are shown) based on Voronoi tessellation and contour detection. (H) Nearest neighbor distance measurement of the astrocytic MAGL blinking events to synaptic release sites labeled by Bassoon. For clarity, thresholded Bassoon voxels were filtered to 300 nm distance from the focal plane (i.e., same volume from where the STORM localization points are detected) and are shown as cyan spheres. (I) Cumulative distribution function of the nearest neighbor distances of astrocytic MAGL blinking events and synaptic release sites between the original and randomized blinking events (n=546 blinking events from 10 images from 3 animals, two-sample Kolmogorov–Smirnov test, d=0.05, p=0.11). (J) Distance distribution of MAGL blinking events to the nearest synaptic release site marked by Bassoon. The same dataset was analyzed as in (I).

Next, we explored if the spatial distribution of the astrocytic MAGL pool has any bias towards the non-astrocytic pool, suggesting a common platform for endocannabinoid degradation. We measured the distance for each astrocytic MAGL blinking event to its nearest non-astrocytic blinking event (intercluster distance between center of masses),

and then repeated this step when astrocytic blinking events were randomized in their respective ROIs. Interestingly, cumulative distribution functions of the intercluster distances were similar between the original and the randomized MAGL blinking event positions, suggesting that there is no preferential targeting of astrocytic MAGL localizations to the non-astrocytic ones (Fig. 10D).

To test whether the distribution of astrocytic MAGL localizations show any preference towards synaptic release sites, we imaged the active zone marker protein Bassoon with confocal resolution (Fig. 10E) and correlated the STORM images of PALE and MAGL with their respective confocal images from the very same field of view (Fig. 10F)[24]. Astrocytic MAGL localizations were segmented and filtered as previously, and for each blinking event we measured the distance to the nearest synapse identified from deconvolved and thresholded images of Bassoon (Fig. 10G, H). When this step was repeated for the randomized MAGL distributions as well, we found that both the original and randomized MAGL localizations had similar distance distributions to synapses (Fig. 10I). The above data therefore show that in contrast to the higher density of non-astrocytic MAGL in the vicinity of Bassoon (Fig. 10J), astrocytic MAGL is not enriched around synapses, suggesting a synapse-independent functional role.

5. Discussion

Astrocytes, once considered merely supportive cells, are now recognized as key regulators of synaptic function, neurovascular coupling, and the brain's immune response. Nanoscale investigations offer unprecedented insights into the intricate molecular and cellular mechanisms underlying astrocyte activity. Probing these cells with high-resolution techniques could uncover the fine structural and molecular changes that may occur during disease progression, providing a clearer understanding of how astrocytes contribute to both neuroprotection and pathology.

5.1. Nanoscale visualization of astrocytes labeled by electroporation

Instead of firing action potentials like neurons, astrocytes display a wide range of dynamic calcium signaling events. Recent data uncovered that the majority of calcium signals do not occur at the somata or large branches[38] but at the spongiform domain that covers ~85% of the astrocytic arbor and is unresolvable by classical light microscopy[89]. Therefore, reconstructing the anatomical and molecular composition of such domains is key to understanding astrocytic communication and their influence on brain function.

Historically, electron microscopy was employed to investigate anatomical structures that are beyond the diffraction limit of classical light microscopy[101]. The required sample preparation steps, fixation and dehydration, however, result in the shrinkage of the extracellular space and introduce artifacts such as the altered astrocytic coverage of synapses[102]. The advent of super-resolution microscopic methods leveraged these specific sample preparation steps. They do not require dehydration and work perfectly well with milder fixation protocols such as immersion fixation that was shown to better preserve the extracellular space[103]. STED was successfully employed to reconstruct the spongiform domain of astrocytes and to identify a compartmentalization model in the so-called nodes that is conceptually similar to that of dendritic spines in neurons[50], providing a structural basis for the tripartite synapse hypothesis[27]. Though offering superior resolution, state-of-the-art STED microscopes still cannot reach the resolution and sensitivity offered by single molecule localization methods. The integrated nanoscale anatomical and molecular measurements therefore still favor SMLM techniques. Nevertheless, combining SMLM with STED for higher resolution of the

correlative imaging modality is a promising direction to benefit from the advantages of both methods[104].

Here, we utilized STORM imaging to reconstruct the architecture of hippocampal astrocytes. The improved resolution resolved thin astrocytic filaments that appeared to be enlarged on confocal microscopic images, and aided the identification of optical artifacts such as the appearance of merged filamentous structures. We imaged astrocytes in brain tissue in their native cellular environment where they retain their intricate morphology, unlike in cell culture systems. The selective and sparse labeling of astrocytes was achieved by postnatal electroporation, which, to the best of our knowledge, has not been used so far to investigate hippocampal astrocytes. Astrocytes may be labeled by alternative methods such as viral injections[45,91]. However, this not only requires careful titration of the virus concentration but the use of transgenic animals to enable astrocyte-specific virus expression. Obtaining knockout animals for a protein of interest would then require double-transgenic animals, whose colony maintenance requires much more care and resources. This holds true for the recently created MORF mice as well where sparse labeling is achieved via genetic mosaicism in a Cre-dependent manner[105]. By contrast, due to the sequential nature of neuro- and then gliogenesis, PALE selectively and sparsely labels astrocytes without the need for any transgenic mouse line. Unlike adeno-associated virus (AAV) mediated gene transfer, the electroporated plasmids do not integrate into the genome. Hence, transcription starts immediately, making it possible to investigate astrocytes right after electroporation, as early as P5[77].

Shifting the timing of electroporation to prenatal ages enables the labeling of other cell types. We labeled radial glia cells *in utero* and employed correlated confocal and STORM imaging to investigate their structure after an adherens junction disruption protocol[78]. These cells develop into neurons, and when combined with PALE, neuron-astrocyte interactions can be visualized in a sparse manner without the use of any transgenic animals or special gene promoters (Zöldi *et al*., unpublished). Moreover, by delaying the *in utero* labeling to E18 and combining it with PALE, or by performing PALE on separate days such as P0 and P1, it is possible to distinguish astrocyte populations that are generated at different timepoints through selective labeling[77]. This could help answer certain neurodevelopmental questions such as whether the timing of gliogenesis affects the spatial distribution or transcriptional profile of astrocytes.

5.2. Dual-color STORM imaging of astrocytes in brain tissue

Parsing molecular data to biological profiles that are beyond the diffraction limit necessitates multicolor SMLM imaging, which is routinely performed in cell culture systems with minimal fluorescent background. However, in native tissue, the challenge arises from the excitation of millions of emitters. Fluorescent background is elevated also due to light scattering, diminishing excitation intensity and reducing the number of photons collected from emission. This issue, along with certain optical aberrations, worsens at greater depths. Hence, many of the fluorophores that have optimal photophysical performance in cell culture systems or various imaging strategies will just not meet the required criteria for STORM imaging in tissue[6].

Multi-color STORM imaging can be implemented in various ways, but each strategy has its own advantages and limitations. An emerging strategy is spectral demixing, where spectrally overlapping fluorophores are excited simultaneously with the same laser line, and a dichroic mirror-based emission splitter separates the overlapping emissions onto distinct regions of the camera chip[106]. Not only chromatic aberration, but the relative drift between channels is also eliminated by the simultaneous imaging scheme. However, splitting the fluorescence emission results in the loss of photons arriving at each camera region, lowering the probability and the precision of their detection. In specimens with lower signal to noise ratio such as thick tissue samples, photon loss may be unacceptable. Multiplexing may also be achieved by elution and re-staining protocols[107]. Here, the final resolution depends also on the registration of images between separate imaging rounds, and the efficiency of fluorophore removal determines channel crosstalk. This is conceptually similar to Exchange-PAINT[9], an alternative SMLM strategy that may become more widely used as much faster imaging can be obtained with newer, optimized oligo sequences[6]. When imaging low copy number targets in biological profiles that have to be abundantly labeled for precise reconstructions, however, even the lowest channel crosstalk can mask important biological data.

Here, we employed spectrally different fluorophores for labeling distinct targets. We show that by carefully adjusting the identification parameters we can achieve crosstalk free imaging. Moreover, even though we used separate laser lines that can result in chromatic aberration and we imaged the specimens in a sequential manner where drift

may arise, on our microscopic setup the two channels did not need additional corrections for perfect alignment. It is worth noting, however, that if introducing a third (green emitting) channel, chromatic aberration may become considerable. Of note, these spectrally different dyes belong to different chemical families and their blinking properties can differ substantially[108,109]. Hence, direct quantitative comparison of the imaged targets is not possible. Lastly, we also acknowledge that the blinking performance of the red emitting CF568 did not match that of the gold-standard far-red-emitting AF647, and much sparser molecular targets than the overexpressed fluorescent proteins in the electroporated astrocytes may only yield discontinuous structures. Optimizing the buffer composition, fluorophore selection and imaging parameters together with the ever-continuing improvements related to STORM imaging have the potential to reduce the limitations of the various multiplexing methods[6,110–112].

We provided examples of differentiating synaptic and astrocytic targets by measuring nearest neighbor distances and colocalization metrics, and using image rotation as a control. However, these methods by themselves cannot filter localization points to the biological profiles of interest. For this reason, we retrieved contours of the astrocytic morphology resulting from the Voronoi tessellation of the anatomical STORM data, and used these two-dimensional contours to filter the molecular STORM data[80,96]. The tessellation process can also be extended to the third, axial dimension[79], and defining the borders of cellular profiles may be achieved via other means such as creating mesh surfaces[113]. As an alternative method, the extracellular matrix can also be visualized via super-resolution shadow imaging (SUSHI)[51,114], where intracellular profiles appear as non-labeled, "negative" structures. By seeing cellular boundaries, super-resolution imaging may unify the advantages of fluorescent light and electron microscopy. Indeed, newer directions such as the bulk labeling of proteins via pan-expansion microscopy aim to provide an ultrastructural context obtained via light microscopy[115].

5.3. Investigating the spatial distribution of astrocytic MAGL

The endocannabinoid-degrading enzyme MAGL has emerged as a promising therapeutic target to control endocannabinoid dynamics and the course of inflammation in the brain [67,68]. While these two biological processes may be coupled to some extent[61], recent data

also suggest that distinct cell types and hence distinct pools of MAGL may be biased for a particular biological function[62], providing a basis for pathway-specific therapies.

In the present study, by using dual-color STORM imaging we were able to reconstruct the morphology of individual hippocampal astrocytes with nanoscale precision and to distinguish between non-astrocytic regions with high and astrocytic regions with low detected MAGL localization-point density. STORM imaging not only provided the resolution required to assign detected MAGL localization points to sub-diffraction-limit astrocytic processes, but also provided sufficient sensitivity to detect the relatively sparse astrocytic MAGL signal, previously missed in electron microscopy studies. Moreover, correlating STORM with confocal imaging could provide a more specific subcellular context, to interpret the astrocytic molecular data in relation to synapses.

In the hippocampal CA1 area both excitatory and inhibitory synapses are equipped with MAGL[74], and therefore the astrocytic regulation of retrograde endocannabinoid signaling may be less important. Our data are consistent with this hypothesis by showing a much lower density of detected MAGL localization points in astrocytic processes than in non-astrocytic regions. Moreover, astrocytic MAGL localizations were not associated with the non-astrocytic ones, nor were they positioned preferentially to presynaptic release sites, arguing against a common platform for endocannabinoid degradation. Importantly, this scenario is consistent with a new study reporting that synaptic 2-AG signals primarily to neurons, whereas astrocytes are engaged by another endocannabinoid, anandamide[116]. The lack of tight control over synaptic endocannabinoid signaling by astrocytes may also be necessary to enable some forms of hippocampal plasticity mechanisms such as heterosynaptic long-term depression that is mediated via the short range spread of retrogradely released endocannabinoids[117]. We cannot rule out the possibility, however, that some hippocampal synaptic connections may be more intensively regulated by astrocytic MAGL, for example via the positioning of perisynaptic astrocytic processes (PAPs)[49]. Indeed, cell type-specific MAGL knockout and rescue experiments showed that astrocytic MAGL can control the time course of endocannabinoid signaling, especially where MAGL is lacking in synaptic terminals regulated by endocannabinoid signaling[62,72,73,118]. Lastly, astrocytic MAGL could also be part of an autonomous endocannabinoid platform: astrocytic CB_1 receptors regulate a

diverse range of brain functions[76], and astrocytes are able to synthesize their own 2-AG as well[119,120].

Which additional rules might dictate the subcellular targeting of MAGL? In light of the dual role of MAGL[61], it is tempting to speculate that the lack of synaptic association for astrocytic MAGL is because these localizations fulfil a different, synapse-independent function that is the production of prostaglandins, particularly PGE_2, which has widespread vasoconstricting effects on parenchymal arterioles via EP1 receptor activation[71]. The astrocyte-specific nanoscale molecular imaging approach presented here will open the way for future studies addressing whether astrocytic MAGL proteins are organized into signalosome nanodomains with the downstream enzymes of the prostaglandin pathway such as the cyclooxygenases[121,122].

Besides neurons there is also an important crosstalk between astrocytes and microglia, especially during inflammation[123]. Of note, astrocyte-specific MAGL deletion alters the mRNA expression profile of inflammation-related genes more intensively in microglia than in astrocytes themselves[124]. Therefore, the fine-tuning of prostaglandin levels may involve complex, multi-cellular pathways mediated by the shuttling of lipid metabolites[62]. How these metabolites are released and whether there are specialized release sites[125,126] for them, however, remains elusive. The shuttling of lipid metabolites may provide an alternative explanation for the role of astrocytic MAGL in the regulation of endocannabinoid signaling. Most studies use 1-5 seconds long depolarization induced suppression of inhibition or excitation (DSI/DSE) as a measure of endocannabinoid dynamics, a protocol which does not mimic physiological endocannabinoid release. In these experiments, astrocyte-specific MAGL knockout mice may show an altered DSI/DSE response simply because of the impaired shuttling and replenishment of those metabolites.

To identify distinct subcellular pools of MAGL, we used an indirect immunolabeling method that introduces an offset between the target molecules and may create false clusters in STORM images. Our recently developed PharmacoSTORM approach[127] that utilizes fluorophore-coupled pharmacoprobes to visualize target-engagement sites with nanometer precision could not only aid the identification of true molecular clusters but could also distinguish between active and non-active enzyme populations. Notably, activity-based fluorescent MAGL probes reliably detected MAGL

both in transfected HEK 293 cells[127] and in brain tissue[128]. We hope that these methodological improvements, combined with our workflow to perform molecular imaging in astrocytes, will help us to better understand astrocytic function in both health and disease.

6. Conclusions

In the current thesis, I presented a method by which glial proteins can be located inside astrocytic processes and demonstrated its strength by exploring the nanoscale distribution of the endocannabinoid-degrading enzyme MAGL specifically in astrocytes.

First, we showed that electroporation is an excellent method to sparsely label various cell types in the brain for subsequent super-resolution reconstruction of their morphology. The advantages of the labeling method are as follows: 1) Electroporation achieves sparse labeling even without the use of any transgenic mice or specific promoters. 2) Various cell types such as radial glia cells, neurons, and astrocytes can be targeted. Postnatal electroporation provides an easy and robust way to label hippocampal astrocytes. 3) The sparse labeling enables cell-specific investigations, possibilities for perturbation models, and provides low fluorescent background in tissue samples. 4) STORM super-resolution imaging can reveal the sub-diffraction-limit architecture of astrocytes in brain tissue.

Second, we demonstrated that dual-color STORM imaging has a sufficient resolution to distinguish between synaptic and astrocytic proteins in brain tissue, and we reached the following conclusions: 1) Careful calibrations of the optical system are required to maintain a high-quality crosstalk- and chromatic aberration free imaging scheme. 2) Nearest neighbor distance and co-localization metrics, combined with control measurements such as rotating images are powerful tools to deduce the cell-specific locations of molecules in the tripartite synapse. We showed that these measures exhibit an opposite behavior when comparing astrocyte- and synapse-specific proteins, such as glutamine synthetase and Bassoon, respectively. 3) A sparse subset of the endocannabinoid-degrading enzyme MAGL is present in hippocampal astrocytes. Voronoi tessellation-based object creation enabled the distinction between astrocytic and non-astrocytic pools of MAGL, and by using tissue samples from MAGL wild type and knockout animals supplemented with imaging controls we verified the specificity of this sparse astrocytic signal. 4) The distribution of astrocytic MAGL favors a synapse-independent role. Correlated confocal and STORM super-resolution imaging revealed that astrocytic MAGL has no preference towards synaptic release sites marked by Bassoon, corroborating previous findings that postulated a role other than the regulation of synaptic endocannabinoid signaling. Taken together, our results highlight the

importance of using sensitive, high-resolution methods to map the spatial arrangement of astrocytic proteins, many of which hold significant clinical relevance.

7. Summary

Although astrocytes are essential to nearly every aspect of brain function, the relationship between the number and distribution of key molecules within astrocytes and their extensive roles remains poorly understood. In this thesis, I provide a brief overview of the key concepts of super-resolution imaging and present a methodology for visualizing astrocytic proteins at the nanoscale level using STORM imaging. I demonstrate the effectiveness of this method by differentiating between astrocytic and non-astrocytic pools of MAGL, a key enzyme in the endocannabinoid signaling pathway with major clinical relevance.

We employed postnatal electroporation to label astrocytes selectively and sparsely in the mouse hippocampus and to reconstruct their architecture with nanoscale precision using STORM. We showed that this level of resolution is a prerequisite to reliably visualize the astrocytic arbor. Moreover, shifting the timing of electroporation enabled the targeting of other cell types such as radial glia. As an added benefit, no transgenic mouse lines or cell type-specific promoters were needed for the sparse labeling that provides low fluorescent background for high-quality super-resolution imaging in tissue.

Then, we demonstrated that dual-color STORM imaging can readily differentiate between synaptic and astrocytic proteins. We performed various control measurements to exclude the possibility of severe optical aberrations, and we presented an analysis workflow based on colocalization and nearest neighbor distance measurements to assign molecules to cells of the tripartite synapse. As a proof of concept, we distinguished between neuronal and astrocytic pools of the endocannabinoid-degrading enzyme monoacylglycerol lipase (MAGL). Our results revealed that a sparse but specific signal of MAGL can be attributed to hippocampal astrocytes, and the enzyme in glial cells does not exhibit any preferential localization toward synapses. This suggests a synapse-independent role, supporting previous findings on astrocytic MAGL's involvement in regulating inflammation rather than the time course of endocannabinoid signaling. With MAGL inhibitors already in clinical trials, our research could have potential clinical implications. Overall, our methodology offers a versatile approach for studying various nanoscale protein distributions in astrocytes in brain tissue preparations.

8. References

1. *Yao Z, van Velthoven CTJ, Kunst M, Zhang M, McMillen D, Lee C, Jung W, Goldy J, Abdelhak A, Aitken M, Baker K, Baker P, Barkan E, Bertagnolli D, Bhandiwad A, Bielstein C, Bishwakarma P, Campos J, Carey D, Casper T, Chakka AB, Chakrabarty R, Chavan S, Chen M, Clark M, Close J, Crichton K, Daniel S, DiValentin P, Dolbeare T, Ellingwood L, Fiabane E, Fliss T, Gee J, Gerstenberger J, Glandon A, Gloe J, Gould J, Gray J, Guilford N, Guzman J, Hirschstein D, Ho W, Hooper M, Huang M, Hupp M, Jin K, Kroll M, Lathia K, Leon A, Li S, Long B, Madigan Z, Malloy J, Malone J, Maltzer Z, Martin N, McCue R, McGinty R, Mei N, Melchor J, Meyerdierks E, Mollenkopf T, Moonsman S, Nguyen TN, Otto S, Pham T, Rimorin C, Ruiz A, Sanchez R, Sawyer L, Shapovalova N, Shepard N, Slaughterbeck C, Sulc J, Tieu M, Torkelson A, Tung H, Valera Cuevas N, Vance S, Wadhwani K, Ward K, Levi B, Farrell C, Young R, Staats B, Wang MQM, Thompson CL, Mufti S, Pagan CM, Kruse L, Dee N, Sunkin SM, Esposito L, Hawrylycz MJ, Waters J, Ng L, Smith K, Tasic B, Zhuang X, Zeng H (2023) A high-resolution transcriptomic and spatial atlas of cell types in the whole mouse brain. Nature **624**, 317–332.*
2. *Werner C, Sauer M, Geis C (2021) Super-resolving Microscopy in Neuroscience. Chem Rev **121**, 11971–12015.*
3. *Maglione M, Sigrist SJ (2013) Seeing the forest tree by tree: super-resolution light microscopy meets the neurosciences. Nat Neurosci **16**, 790–7.*
4. *Hell SW (2007) Far-field optical nanoscopy. Science **316**, 1153–8.*
5. *Huang B, Babcock H, Zhuang X (2010) Breaking the diffraction barrier: Super-resolution imaging of cells. Cell **143**, 1047–1058.*
6. *Lelek M, Gyparaki MT, Beliu G, Schueder F, Griffié J, Manley S, Jungmann R, Sauer M, Lakadamyali M, Zimmer C (2021) Single-molecule localization microscopy. Nature Reviews Methods Primers **1**, 1–39.*
7. *Rust MJ, Bates M, Zhuang X (2006) Sub-diffraction-limit imaging by stochastic optical reconstruction microscopy (STORM). Nat Methods **3**, 793–795.*

8. *Betzig E, Patterson GH, Sougrat R, Lindwasser OW, Olenych S, Bonifacino JS, Davidson M, Lippincott-Schwartz J, Hess HF (2006) Imaging intracellular fluorescent proteins at nanometer resolution. Science **313**, 1642–1645.*
9. *Jungmann R, Avendaño MS, Woehrstein JB, Dai M, Shih WM, Yin P (2014) Multiplexed 3D cellular super-resolution imaging with DNA-PAINT and Exchange-PAINT. Nat Methods **11**, 313–318.*
10. *Tam J, Merino D (2015) Stochastic optical reconstruction microscopy (STORM) in comparison with stimulated emission depletion (STED) and other imaging methods. J Neurochem **135**, 643–658.*
11. *Nicovich PR, Owen DM, Gaus K (2017) Turning single-molecule localization microscopy into a quantitative bioanalytical tool. Nat Protoc **12**, 453–461.*
12. *Jacquemet G, Carisey AF, Hamidi H, Henriques R, Leterrier C (2020) The cell biologist's guide to super-resolution microscopy. J Cell Sci **133**, jcs240713.*
13. *Valli J, Garcia-Burgos A, Rooney LM, de Melo e Oliveira BV, Duncan RR, Rickman C (2021) Seeing beyond the limit: A guide to choosing the right super-resolution microscopy technique. Journal of Biological Chemistry **297**, 100791.*
14. *Balzarotti F, Eilers Y, Gwosch KC, Gynnå AH, Westphal V, Stefani FD, Elf J, Hell SW (2017) Nanometer resolution imaging and tracking of fluorescent molecules with minimal photon fluxes. Science **355**, 606–612.*
15. *Sauer M, Heilemann M (2017) Single-molecule localization microscopy in eukaryotes. Chem Rev **117**, 7478–7509.*
16. *Baddeley D, Bewersdorf J (2017) Biological insight from super-resolution microscopy: what we can learn from localization-based images. Annu Rev Biochem **87**, 965–989.*
17. *Dani A, Huang B, Bergan J, Dulac C, Zhuang X (2010) Superresolution imaging of chemical synapses in the brain. Neuron **68**, 843–856.*

18. *MacGillavry HD, Song Y, Raghavachari S, Blanpied TA (2013) Nanoscale scaffolding domains within the postsynaptic density concentrate synaptic AMPA receptors. Neuron **78**, 615–622.*

19. *Nair D, Hosy E, Petersen JD, Constals A, Giannone G, Choquet D, Sibarita J-B (2013) Super-resolution imaging reveals that AMPA receptors inside synapses are dynamically organized in nanodomains regulated by PSD95. Journal of Neuroscience **33**, 13204–13224.*

20. *Kellermayer B, Ferreira JS, Dupuis J, Levet F, Grillo-Bosch D, Bard L, Linarès-Loyez J, Bouchet D, Choquet D, Rusakov DA, Bon P, Sibarita JB, Cognet L, Sainlos M, Carvalho AL, Groc L (2018) Differential nanoscale topography and functional role of GluN2-NMDA receptor subtypes at glutamatergic synapses. Neuron **100**, 106-119.e7.*

21. *Tang A-H, Chen H, Li TP, Metzbower SR, MacGillavry HD, Blanpied TA (2016) A trans-synaptic nanocolumn aligns neurotransmitter release to receptors. Nature **536**, 210–214.*

22. *Crosby KC, Gookin SE, Garcia JD, Hahm KM, Dell'Acqua ML, Smith KR (2019) Nanoscale subsynaptic domains underlie the organization of the inhibitory synapse. Cell Rep **26**, 3284-3297.e3.*

23. *Rahbek-Clemmensen T, Lycas MD, Erlendsson S, Eriksen J, Apuschkin M, Vilhardt F, Jørgensen TN, Hansen FH, Gether U (2017) Super-resolution microscopy reveals functional organization of dopamine transporters into cholesterol and neuronal activity-dependent nanodomains. Nat Commun **8**, 740.*

24. *Barna L, Dudok B, Miczán V, Horváth A, László Z, Katona I (2016) Correlated confocal and super-resolution imaging by VividSTORM. Nat Protoc **11**, 163–183.*

25. *Dudok B, Barna L, Ledri M, Szabó SI, Szabadits E, Pintér B, Woodhams SG, Henstridge CM, Balla GY, Nyilas R, Varga C, Lee SHS-H, Matolcsi M, Cervenak J, Kacskovics I, Watanabe M, Sagheddu C, Melis M, Pistis M, Soltesz I, Katona I (2015) Cell-specific STORM super-resolution imaging reveals nanoscale organization of cannabinoid signaling. Nat Neurosci **18**, 75–86.*

26. *Zöldi M, Katona I (2023) STORM super-resolution imaging of CB1 receptors in tissue preparations. Methods in Molecular Biology **2576**, 437–451.*
27. *Araque A, Parpura V, Sanzgiri RP, Haydon PG (1999) Tripartite synapses: Glia, the unacknowledged partner. Trends Neurosci **22**, 208–215.*
28. *Verkhratsky A, Nedergaard M (2018) Physiology of astroglia. Physiol Rev **98**, 239–389.*
29. *Khakh BS (2025) On astrocyte-neuron interactions: Broad insights from the striatum. Neuron **113**, 3079–3107.*
30. *Lee HG, Wheeler MA, Quintana FJ (2022) Function and therapeutic value of astrocytes in neurological diseases. Nat Rev Drug Discov **21**, 339–358.*
31. *Brandebura AN, Paumier A, Onur TS, Allen NJ (2022) Astrocyte contribution to dysfunction, risk and progression in neurodegenerative disorders. Nat Rev Neurosci **24**, 23–39.*
32. *Lee HG, Lee JH, Flausino LE, Quintana FJ (2023) Neuroinflammation: An astrocyte perspective. Sci Transl Med **15**, eadi7828.*
33. *Arizono M, Nägerl UV (2022) Deciphering the functional nano-anatomy of the tripartite synapse using stimulated emission depletion microscopy. Glia **70**, 607–618.*
34. *Aleksejenko N, Heller JP (2021) Super-resolution imaging to reveal the nanostructure of tripartite synapses. Neuronal Signal **5**, 1–12.*
35. *Heller JP, Rusakov DA (2015) Morphological plasticity of astroglia: Understanding synaptic microenvironment. Glia **63**, 2133–2151.*
36. *Yu X, Nagai J, Khakh BS (2020) Improved tools to study astrocytes. Nat Rev Neurosci **21**, 121–138.*
37. *Baldwin KT, Murai KK, Khakh BS (2024) Astrocyte morphology. Trends Cell Biol **34**, 547–565.*
38. *Bindocci E, Savtchouk I, Liaudet N, Becker D, Carriero G, Volterra A (2017) Three-dimensional Ca2+ imaging advances understanding of astrocyte biology. Science **356**, eaai8185.*
39. *Cahoy JD, Emery B, Kaushal A, Foo LC, Zamanian JL, Christopherson KS, Xing Y, Lubischer JL, Krieg PA, Krupenko SA, Thompson WJ, Barres BA*

(2008) A transcriptome database for astrocytes, neurons, and oligodendrocytes: A new resource for understanding brain development and function. Journal of Neuroscience ***28****, 264–278.*

40. *Escartin C, Galea E, Lakatos A, O'Callaghan JP, Petzold GC, Serrano-Pozo A, Steinhäuser C, Volterra A, Carmignoto G, Agarwal A, Allen NJ, Araque A, Barbeito L, Barzilai A, Bergles DE, Bonvento G, Butt AM, Chen WT, Cohen-Salmon M, Cunningham C, Deneen B, De Strooper B, Díaz-Castro B, Farina C, Freeman M, Gallo V, Goldman JE, Goldman SA, Götz M, Gutiérrez A, Haydon PG, Heiland DH, Hol EM, Holt MG, Iino M, Kastanenka K V., Kettenmann H, Khakh BS, Koizumi S, Lee CJ, Liddelow SA, MacVicar BA, Magistretti P, Messing A, Mishra A, Molofsky A V., Murai KK, Norris CM, Okada S, Oliet SHR, Oliveira JF, Panatier A, Parpura V, Pekna M, Pekny M, Pellerin L, Perea G, Pérez-Nievas BG, Pfrieger FW, Poskanzer KE, Quintana FJ, Ransohoff RM, Riquelme-Perez M, Robel S, Rose CR, Rothstein JD, Rouach N, Rowitch DH, Semyanov A, Sirko S, Sontheimer H, Swanson RA, Vitorica J, Wanner IB, Wood LB, Wu J, Zheng B, Zimmer ER, Zorec R, Sofroniew M V., Verkhratsky A (2021) Reactive astrocyte nomenclature, definitions, and future directions. Nat Neurosci* ***24****, 312–325.*

41. *Habib N, McCabe C, Medina S, Varshavsky M, Kitsberg D, Dvir-Szternfeld R, Green G, Dionne D, Nguyen L, Marshall JL, Chen F, Zhang F, Kaplan T, Regev A, Schwartz M (2020) Disease-associated astrocytes in Alzheimer's disease and aging. Nat Neurosci* ***23****, 701–706.*

42. *O'Dea MR, Hasel P (2025) Are we there yet? Exploring astrocyte heterogeneity one cell at a time. Glia* ***73****, 619–631.*

43. *Chai H, Diaz-Castro B, Shigetomi E, Monte E, Octeau JC, Yu X, Cohn W, Rajendran PS, Vondriska TM, Whitelegge JP, Coppola G, Khakh BS (2017) Neural circuit-specialized astrocytes: transcriptomic, proteomic, morphological, and functional evidence. Neuron* ***95****, 531–549.*

44. *Soto JS, Jami-Alahmadi Y, Chacon J, Moye SL, Diaz-Castro B, Wohlschlegel JA, Khakh BS (2023) Astrocyte–neuron subproteomes and obsessive–compulsive disorder mechanisms. Nature* ***616****, 764–773.*

45. *Sakers K, Lake AM, Khazanchi R, Ouwenga R, Vasek MJ, Dani A, Dougherty JD (2017) Astrocytes locally translate transcripts in their peripheral processes. Proceedings of the National Academy of Sciences **114**, E3830–E3838.*

46. *Heller JP, Michaluk P, Sugao K, Rusakov DA (2017) Probing nano-organization of astroglia with multi-color super-resolution microscopy. J Neurosci Res **95**, 2159–2171.*

47. *Heller JP, Odii T, Zheng K, Rusakov DA (2020) Imaging tripartite synapses using super-resolution microscopy. Methods **174**, 81–90.*

48. *Michaluk P, Heller JP, Rusakov DA (2021) Rapid recycling of glutamate transporters on the astroglial surface. Elife **10**, 1–23.*

49. *Henneberger C, Bard L, Panatier A, Reynolds JP, Kopach O, Medvedev NI, Minge D, Herde MK, Anders S, Kraev I, Heller JP, Rama S, Zheng K, Jensen TP, Sanchez-Romero I, Jackson CJ, Janovjak H, Ottersen OP, Nagelhus EA, Oliet SHR, Stewart MG, Nägerl UV, Rusakov DA (2020) LTP induction boosts glutamate spillover by driving withdrawal of perisynaptic astroglia. Neuron **108**, 919–936.*

50. *Arizono M, Inavalli VVGK, Panatier A, Pfeiffer T, Angibaud J, Levet F, Ter Veer MJT, Stobart J, Bellocchio L, Mikoshiba K, Marsicano G, Weber B, Oliet SHR, Nägerl UV (2020) Structural basis of astrocytic Ca2+ signals at tripartite synapses. Nat Commun **11**, 1906.*

51. *Arizono M, Inavalli VVGK, Bancelin S, Fernández-Monreal M, Nägerl UV (2021) Super-resolution shadow imaging reveals local remodeling of astrocytic microstructures and brain extracellular space after osmotic challenge. Glia **69**, 1605–1613.*

52. *Aten S, Kiyoshi CM, Arzola EP, Patterson JA, Taylor AT, Du Y, Guiher AM, Philip M, Camacho EG, Mediratta D, Collins K, Boni K, Garcia SA, Kumar R, Drake AN, Hegazi A, Trank L, Benson E, Kidd G, Terman D, Zhou M (2022) Ultrastructural view of astrocyte arborization, astrocyte-astrocyte and astrocyte-synapse contacts, intracellular vesicle-like structures, and mitochondrial network. Prog Neurobiol **213**, 102264.*

53. *Stogsdill JA, Ramirez J, Liu D, Kim YH, Baldwin KT, Enustun E, Ejikeme T, Ji RR, Eroglu C (2017) Astrocytic neuroligins control astrocyte morphogenesis and synaptogenesis. Nature **551**, 192–197.*

54. *Katona I, Freund TF (2012) Multiple functions of endocannabinoid signaling in the brain. Annu Rev Neurosci **35**, 529–558.*

55. *Lu H-C, Mackie K (2016) An introduction to the endogenous cannabinoid system. Biol Psychiatry **79**, 516–525.*

56. *Katona I, Freund TF (2008) Endocannabinoid signaling as a synaptic circuit breaker in neurological disease. Nat Med **14**, 923–930.*

57. *Di Marzo V (2018) New approaches and challenges to targeting the endocannabinoid system. Nat Rev Drug Discov **17**, 623–639.*

58. *Long JZ, Li W, Booker L, Burston JJ, Kinsey SG, Schlosburg JE, Pavón FJ, Serrano AM, Selley DE, Parsons LH, Lichtman AH, Cravatt BF (2008) Selective blockade of 2-arachidonoylglycerol hydrolysis produces cannabinoid behavioral effects. Nat Chem Biol **5**, 37–44.*

59. *Blankman JL, Simon GM, Cravatt BF (2007) A comprehensive profile of brain enzymes that hydrolyze the endocannabinoid 2-arachidonoylglycerol. Chem Biol **14**, 1347–1356.*

60. *Long JZ, Nomura DK, Cravatt BF (2009) Characterization of Monoacylglycerol Lipase Inhibition Reveals Differences in Central and Peripheral Endocannabinoid Metabolism. Chem Biol **16**, 744–753.*

61. *Nomura DK, Morrison BE, Blankman JL, Long JZ, Kinsey SG, Marcondes MCG, Ward AM, Hahn YK, Lichtman AH, Conti B, Cravatt BF (2011) Endocannabinoid hydrolysis generates brain prostaglandins that promote neuroinflammation. Science **334**, 809–813.*

62. *Viader A, Blankman JL, Zhong P, Liu X, Schlosburg JE, Joslyn CM, Liu QS, Tomarchio AJ, Lichtman AH, Selley DE, Sim-Selley LJ, Cravatt BF (2015) Metabolic interplay between astrocytes and neurons regulates endocannabinoid action. Cell Rep **12**, 798–808.*

63. *Grabner GF, Eichmann TO, Wagner B, Gao Y, Farzi A, Taschler U, Radner FPW, Schweiger M, Lass A, Holzer P, Zinser E, Tschöp MH, Yi CX, Zimmermann R, Tschöp MH, Yi CX, Zimmermann R (2016) Deletion of*

*monoglyceride lipase in astrocytes attenuates lipopolysaccharide-induced neuroinflammation. Journal of Biological Chemistry **291**, 913–923.*

64. *Hu M, Zhu D, Zhang J, Gao F, Hashem J, Kingsley P, Marnett LJ, MacKie K, Chen C (2022) Enhancing endocannabinoid signalling in astrocytes promotes recovery from traumatic brain injury. Brain **145**, 179–193.*
65. *Ruiz-Calvo A, Bajo-Grañeras R, Maroto IB, Zian D, Grabner GF, García-Taboada E, Resel E, Zechner R, Zimmermann R, Ortega-Gutiérrez S, Galve-Roperh I, Bellocchio L, Guzmán M (2019) Astroglial monoacylglycerol lipase controls mutant huntingtin-induced damage of striatal neurons. Neuropharmacology **150**, 134–144.*
66. *Schlosburg JE, Blankman JL, Long JZ, Nomura DK, Pan B, Kinsey SG, Nguyen PT, Ramesh D, Booker L, Burston JJ, Thomas EA, Selley DE, Sim-Selley LJ, Liu QS, Lichtman AH, Cravatt BF (2010) Chronic monoacylglycerol lipase blockade causes functional antagonism of the endocannabinoid system. Nat Neurosci **13**, 1113–1119.*
67. *Alhouayek M, Masquelier J, Muccioli GG (2014) Controlling 2-arachidonoylglycerol metabolism as an anti-inflammatory strategy. Drug Discov Today **19**, 295–304.*
68. *Grabner GF, Zimmermann R, Schicho R, Taschler U (2017) Monoglyceride lipase as a drug target: At the crossroads of arachidonic acid metabolism and endocannabinoid signaling. Pharmacol Ther **175**, 35–46.*
69. *Chen R, Zhang J, Wu Y, Wang D, Feng G, Tang Y-P, Teng Z, Chen C (2012) Monoacylglycerol lipase is a therapeutic target for Alzheimer's disease. Cell Rep **2**, 1329–1339.*
70. *Piro JR, Benjamin DI, Duerr JM, Pi Y, Gonzales C, Wood KM, Schwartz JW, Nomura DK, Samad TA (2012) A dysregulated endocannabinoid-eicosanoid network supports pathogenesis in a mouse model of Alzheimer's disease. Cell Rep **1**, 617–623.*
71. *Farrell JS, Colangeli R, Dong A, George AG, Addo-Osafo K, Kingsley PJ, Morena M, Wolff MD, Dudok B, He K, Patrick TA, Sharkey KA, Patel S, Marnett LJ, Hill MN, Li Y, Teskey GC, Soltesz I (2021) In vivo*

*endocannabinoid dynamics at the timescale of physiological and pathological neural activity. Neuron **109**, 2398-2403.e4.*

72. *Uchigashima M, Yamazaki M, Yamasaki M, Tanimura A, Sakimura K, Kano M, Watanabe M (2011) Molecular and morphological configuration for 2-Arachidonoylglycerol-mediated retrograde signaling at mossy cell-granule cell synapses in the dentate gyrus. Journal of Neuroscience **31**, 7700–7714.*
73. *Tanimura A, Uchigashima M, Yamazaki M, Uesaka N, Mikuni T, Abe M, Hashimoto K, Watanabe M, Sakimura K, Kano M (2012) Synapse type-independent degradation of the endocannabinoid 2-arachidonoylglycerol after retrograde synaptic suppression. Proceedings of the National Academy of Sciences **109**, 12195–12200.*
74. *Gulyas AI, Cravatt BF, Bracey MH, Dinh TP, Piomelli D, Boscia F, Freund TF (2004) Segregation of two endocannabinoid-hydrolyzing enzymes into pre- and postsynaptic compartments in the rat hippocampus, cerebellum and amygdala. European Journal of Neuroscience **20**, 441–458.*
75. *Ludányi A, Hu SSJ, Yamazaki M, Tanimura A, Piomelli D, Watanabe M, Kano M, Sakimura K, Maglóczky Z, Mackie K, Freund TF, Katona I (2011) Complementary synaptic distribution of enzymes responsible for synthesis and inactivation of the endocannabinoid 2-arachidonoylglycerol in the human hippocampus. Neuroscience **174**, 50–63.*
76. *Eraso-Pichot A, Pouvreau S, Olivera-Pinto A, Gomez-Sotres P, Skupio U, Marsicano G (2023) Endocannabinoid signaling in astrocytes. Glia **71**, 44–59.*
77. *Zöldi M, Katona I (2026) A super-resolution approach for astrocyte-specific molecular imaging reveals the nanoscale distribution of monoacylglycerol lipase, the metabolic node between endocannabinoid and prostaglandin signaling. Glia **74**, e70186.*
78. *László ZI, Lele Z, Zöldi M, Miczán V, Mógor F, Simon GM, Mackie K, Kacskovics I, Cravatt BF, Katona I (2020) ABHD4-dependent developmental anoikis safeguards the embryonic brain. Nat Commun **11**, 4363.*

79. *Levet F, Julien G, Galland R, Butler C, Beghin A, Chazeau A, Hoess P, Ries J, Giannone G, Sibarita J-B (2019) Coloc-Tesseler: a tessellation-based colocalization analysis for single-molecule localization microscopy. Nat Commun **10**, 2379.*

80. *Levet F, Hosy E, Kechkar A, Butler C, Beghin A, Choquet D, Sibarita JB (2015) SR-Tesseler: A method to segment and quantify localization-based super-resolution microscopy data. Nat Methods **12**, 1065–1071.*

81. *Kriegstein A, Alvarez-Buylla A (2009) The Glial Nature of Embryonic and Adult Neural Stem Cells. Annu Rev Neurosci **32**, 149–184.*

82. *Klingler E, Francis F, Jabaudon D, Cappello S (2021) Mapping the molecular and cellular complexity of cortical malformations. Science **371**, eaba4517.*

83. *Kawauchi T, Sekine K, Shikanai M, Chihama K, Tomita K, Kubo K ichiro, Nakajima K, Nabeshima Y ichi, Hoshino M (2010) Rab GTPases-dependent endocytic pathways regulate neuronal migration and maturation through N-cadherin trafficking. Neuron **67**, 588–602.*

84. *Lo Turco J, Manent JB, Sidiqi F (2009) New and improved tools for in utero electroporation studies of developing cerebral cortex. Cerebral Cortex **19**, i120–i125.*

85. *Boutin C, Diestel S, Desoeuvre A, Tiveron MC, Cremer H (2008) Efficient in vivo electroporation of the postnatal rodent forebrain. PLoS One **3**, e1883.*

86. *Ge WP, Miyawaki A, Gage FH, Jan YN, Jan LY (2012) Local generation of glia is a major astrocyte source in postnatal cortex. Nature **484**, 376–380.*

87. *Wang X, Chang L, Guo Z, Li W, Liu W, Cai B, Wang J (2013) Neonatal SVZ EGFP-labeled cells produce neurons in the olfactory bulb and astrocytes in the cerebral cortex by in-vivo electroporation. Neuroreport **24**, 381–387.*

88. *Baumgart J, Baumgart N (2016) Cortex-, hippocampus-, thalamus-, hypothalamus-, lateral septal nucleus-and striatum-specific in utero electroporation in the C57BL/6 mouse. Journal of Visualized Experiments e53303.*

89. *Bushong EA, Martone ME, Jones YZ, Ellisman MH (2002) Protoplasmic astrocytes in CA1 stratum radiatum occupy separate anatomical domains. Journal of Neuroscience* ***22****, 183–192.*

90. *Shigetomi E, Bushong EA, Haustein MD, Tong X, Jackson-Weaver O, Kracun S, Xu J, Sofroniew M V., Ellisman MH, Khakh BS (2013) Imaging calcium microdomains within entire astrocyte territories and endfeet with GCaMPs expressed using adeno-associated viruses. Journal of General Physiology* ***141****, 633–647.*

91. *Srinivasan R, Lu TY, Chai H, Xu J, Huang BS, Golshani P, Coppola G, Khakh BS (2016) New transgenic mouse lines for selectively targeting astrocytes and studying calcium signals in astrocyte processes in situ and in vivo. Neuron* ***92****, 1181–1195.*

92. *Salmon CK, Syed TA, Kacerovsky JB, Alivodej N, Schober AL, Sloan TFW, Pratte MT, Rosen MP, Green M, Chirgwin-Dasgupta A, Mehta S, Jilani A, Wang Y, Vali H, Mandato CA, Siddiqi K, Murai KK (2023) Organizing principles of astrocytic nanoarchitecture in the mouse cerebral cortex. Current Biology* ***33****, 957-972.e5.*

93. *Derouiche A, Frotscher M (1991) Astroglial processes around identified glutamatergic synapses contain glutamine synthetase: evidence for transmitter degradation. Brain Res* ***552****, 346–350.*

94. *Octeau JC, Chai H, Jiang R, Bonanno SL, Martin KC, Khakh BS (2018) An optical neuron-astrocyte proximity assay at synaptic distance scales. Neuron* ***98****, 49–66.*

95. *Chaudhry FA, Lehre KP, Lookeren Campagne M van, Ottersen OP, Danbolt NC, Storm-Mathisen J (1995) Glutamate transporters in glial plasma membranes: Highly differentiated localizations revealed by quantitative ultrastructural immunocytochemistry. Neuron* ***15****, 711–720.*

96. *Lycas MD, Ejdrup AL, Sørensen AT, Haahr NO, Jørgensen SH, Guthrie DA, Støier JF, Werner C, Newman AH, Sauer M, Herborg F, Gether U (2022) Nanoscopic dopamine transporter distribution and conformation are inversely regulated by excitatory drive and D2 autoreceptor activity. Cell Rep* ***40****, 111431.*

97. *Veatch SL, Machta BB, Shelby SA, Chiang EN, Holowka DA, Baird BA (2012) Correlation functions quantify super-resolution images and estimate apparent clustering due to over-counting. PLoS One **7**, e31457.*

98. *Baumgart F, Arnold AM, Leskovar K, Staszek K, Fölser M, Weghuber J, Stockinger H, Schütz GJ (2016) Varying label density allows artifact-free analysis of membrane-protein nanoclusters. Nat Methods **13**, 661–664.*

99. *Siddig S, Aufmkolk S, Doose S, Jobin ML, Werner C, Sauer M, Calebiro D (2020) Super-resolution imaging reveals the nanoscale organization of metabotropic glutamate receptors at presynaptic active zones. Sci Adv **6**, eaay7193.*

100. *Ester M, Kriegel H-P, Sander J, Xu X (1996) A density-based algorithm for discovering clusters in large spatial databases with noise. Proc 2nd Int Conf Knowl Discov Data Min **96**, 226–231.*

101. *Ventura R, Harris KM (1999) Three-dimensional relationships between hippocampal synapses and astrocytes. Journal of Neuroscience **19**, 6897–6906.*

102. *Korogod N, Petersen CC, Knott GW (2015) Ultrastructural analysis of adult mouse neocortex comparing aldehyde perfusion with cryo fixation. Elife **4**, 1–17.*

103. *Idziak A, Inavalli VVGK, Bancelin S, Arizono M, Nägerl UV (2023) The impact of chemical fixation on the microanatomy of mouse organotypic hippocampal slices. eNeuro **10**, 1–9.*

104. *Inavalli VVGK, Lenz MO, Butler C, Angibaud J, Compans B, Levet F, Tønnesen J, Rossier O, Giannone G, Thoumine O, Hosy E, Choquet D, Sibarita JB, Nägerl UV (2019) A super-resolution platform for correlative live single-molecule imaging and STED microscopy. Nat Methods **16**, 1263–1268.*

105. *Veldman MB, Park CS, Eyermann CM, Zhang JY, Zuniga-Sanchez E, Hirano AA, Daigle TL, Foster NN, Zhu M, Langfelder P, Lopez IA, Brecha NC, Zipursky SL, Zeng H, Dong H, Yang XW (2020) Brainwide genetic sparse cell labeling to illuminate the morphology of neurons and glia with cre-dependent MORF mice. Neuron **108**, 111–127.*

106. *Lampe A, Haucke V, Sigrist SJ, Heilemann M, Schmoranzer J (2012) Multi-colour direct STORM with red emitting carbocyanines. Biol Cell* ***104****, 229–237.*

107. *Klevanski M, Herrmannsdoerfer F, Venkataramani V, Sass S, Heilemann M, Kuner T (2019) Automated highly multiplexed super-resolution imaging of protein nano-architecture in cells and tissues. Nat Commun* ***11****, 1552.*

108. *Lehmann M, Lichtner G, Klenz H, Schmoranzer J (2016) Novel organic dyes for multicolor localization-based super-resolution microscopy. J Biophotonics* ***9****, 161–170.*

109. *Dempsey GT, Vaughan JC, Hao Chen K, Bates M, Zhuang X (2011) Evaluation of fluorophores for optimal performance in. Nat Methods* ***8****, 1027–1036.*

110. *Beghin A, Kechkar A, Butler C, Levet F, Cabillic M, Rossier O, Giannone G, Galland R, Choquet D, Sibarita JB (2017) Localization-based super-resolution imaging meets high-content screening. Nat Methods* ***14****, 1184–1190.*

111. *Diekmann R, Kahnwald M, Schoenit A, Deschamps J, Matti U, Ries J (2020) Optimizing imaging speed and excitation intensity for single-molecule localization microscopy. Nat Methods* ***17****, 909–912.*

112. *Thevathasan JV, Kahnwald M, Cieśliński K, Hoess P, Peneti SK, Reitberger M, Heid D, Kasuba KC, Hoerner SJ, Li Y, Wu Y Le, Mund M, Matti U, Pereira PM, Henriques R, Nijmeijer B, Kueblbeck M, Sabinina VJ, Ellenberg J, Ries J (2019) Nuclear pores as versatile reference standards for quantitative superresolution microscopy. Nat Methods* ***16****, 1045–1053.*

113. *Marin Z, Graff M, Barentine AES, Soeller C, Chung KKH, Fuentes LA, Baddeley D (2021) PYMEVisualize: an open-source tool for exploring 3D super-resolution data. Nat Methods* ***18****, 582–584.*

114. *Tønnesen J, Inavalli VVGK, Nägerl UV (2018) Super-resolution imaging of the extracellular space in living brain tissue. Cell* ***172****, 1108-1121.e15.*

115. *M'Saad O, Bewersdorf J (2020) Light microscopy of proteins in their ultrastructural context. Nat Commun* ***11****, 3850.*

116. *Noriega-Prieto JA, Falcón-Moya R, Noeker JA, Cai R, Fundazuri UB, Eraso-Pichot A, Cai S, Guttipatti P, Belisle L, Rodríguez-Moreno A, van der Stelt M, Li Y, Cheer JF, Marsicano G, Kofuji P, Araque A (2026) Distinct endocannabinoids specifically signal to astrocytes or neurons in the adult mouse hippocampus. Nat Neurosci **29**, 445–454.*

117. *Chevaleyre V, Castillo PE (2003) Heterosynaptic LTD of hippocampal GABAergic synapses: A novel role of endocannabinoids in regulating excitability. Neuron **38**, 461–472.*

118. *Liu X, Chen Y, Vickstrom CR, Li Y, Viader A, Cravatt BF, Liu QS (2016) Coordinated regulation of endocannabinoid-mediated retrograde synaptic suppression in the cerebellum by neuronal and astrocytic monoacylglycerol lipase. Sci Rep **6**, 1–10.*

119. *Walter L, Dinh T, Stella N (2004) ATP induces a rapid and pronounced increase in 2-arachidonoylglycerol production by astrocytes, a response limited by monoacylglycerol lipase. Journal of Neuroscience **24**, 8068–8074.*

120. *Hegyi Z, Oláh T, Kőszeghy Á, Pisticelli F, Holló K, Pál B, Csernoch L, Di Marzo V, Antal M (2018) CB1 receptor activation induces intracellular Ca2+ mobilization and 2-arachidonoylglycerol release in rodent spinal cord astrocytes. Sci Rep **8**, 1–16.*

121. *Dócs K, Hegyi Z, Holló K, Kis G, Hegedűs K, Antal M (2015) Selective axonal and glial distribution of monoacylglycerol lipase immunoreactivity in the superficial spinal dorsal horn of rodents. Brain Struct Funct **220**, 2625–2637.*

122. *Dócs K, Balázs A, Papp I, Szücs P, Hegyi Z (2024) Reactive spinal glia convert 2-AG to prostaglandins to drive aberrant astroglial calcium signaling. Front Cell Neurosci **18**, 1–17.*

123. *Linnerbauer M, Wheeler MA, Quintana FJ (2020) Astrocyte Crosstalk in CNS Inflammation. Neuron **108**, 608–622.*

124. *Zhu D, Zhang J, Hashem J, Gao F, Chen C (2023) Inhibition of 2-arachidonoylglycerol degradation enhances glial immunity by single-cell transcriptomic analysis. J Neuroinflammation **20**, 1–17.*

125. *Cheung G, Bataveljic D, Visser J, Kumar N, Moulard J, Dallérac G, Mozheiko D, Rollenhagen A, Ezan P, Mongin C, Chever O, Bemelmans AP, Lübke J, Leray I, Rouach N (2022) Physiological synaptic activity and recognition memory require astroglial glutamine. Nat Commun **13**, 753.*

126. *de Ceglia R, Ledonne A, Litvin DG, Lind BL, Carriero G, Latagliata EC, Bindocci E, Di Castro MA, Savtchouk I, Vitali I, Ranjak A, Congiu M, Canonica T, Wisden W, Harris K, Mameli M, Mercuri N, Telley L, Volterra A (2023) Specialized astrocytes mediate glutamatergic gliotransmission in the CNS. Nature **622**, 120–129.*

127. *Prokop S, Ábrányi-Balogh P, Barti B, Vámosi M, Zöldi M, Barna L, Urbán GM, Tóth AD, Dudok B, Egyed A, Deng H, Leggio GM, Hunyady L, van der Stelt M, Keserű GM, Katona I (2021) PharmacoSTORM nanoscale pharmacology reveals cariprazine binding on Islands of Calleja granule cells. Nat Commun **12**, 6505.*

128. *Vliet D van der, Klinkenberg AXY, Platte R, Higgins K, Prokop S, Huizenga MCW, Kraaijevanger L, Egmond N van, Straub VM, Kole MHP, Pacher P, Katona I, Huitinga I, Stelt M van der (2025) Spatially Resolved Mapping of Monoacylglycerol Lipase Activity in the Brain. ACS Chem Neurosci **16**, 4622–4635.*

9. Bibliography of the candidate's publications

Publications related to the thesis:

1. **Zöldi M**, Katona I (2026) A super-resolution approach for astrocyte-specific molecular imaging reveals the nanoscale distribution of monoacylglycerol lipase, the metabolic node between endocannabinoid and prostaglandin signaling. *Glia* 74, e70186.

2. **Zöldi M**, Katona I (2023) STORM super-resolution imaging of CB1 receptors in tissue preparations. *Methods in Molecular Biology* 2576, 437–451.

3. László ZI, Lele Z, **Zöldi M**, Miczán V, Mógor F, Simon GM, Mackie K, Kacskovics I, Cravatt BF, Katona I (2020) ABHD4-dependent developmental anoikis safeguards the embryonic brain. *Nat Commun* 11, 4363.

Publications unrelated to the thesis:

1. Barti B, Dudok B, Kenesei K, **Zöldi M**, Miczán V, Balla GY, Zala D, Tasso M, Sagheddu C, Kisfali M, Tóth B, Ledri M, Sylvester Vizi E, Melis M, Barna L, Lenkei Z, Soltész I, Katona I (2024) Presynaptic nanoscale components of retrograde synaptic signaling. *Sci Adv* 10, eado0077.

2. Hughes HQ, Floyd KA, Hossain S, Anantharaman S, Kysela DT, **Zöldi M**, Banra L, Yu Y, Kappler MP, Dalia TN, Podicheti RC, Rusch DB, Zhuang M, Fraser CL, Brun Y V, Jacobson SC, Mckinlay JB, Yildiz FH, Boon EM, Dalia AB (2022) Nitric oxide stimulates type IV MSHA pilus retraction in Vibrio cholerae via activation of the phosphodiesterase CdpA. *Proceedings of the National Academy of Sciences* 119, e2108349119.

3. Prokop S, Ábrányi-Balogh P, Barti B, Vámosi M, **Zöldi M**, Barna L, Urbán GM, Tóth AD, Dudok B, Egyed A, Deng H, Leggio GM, Hunyady L, van der Stelt M, Keserű GM, Katona I (2021) PharmacoSTORM nanoscale pharmacology reveals cariprazine binding on Islands of Calleja granule cells. *Nat Commun* 12, 6505.

4. Klein PM, Parihar VK, Szabo GG, **Zöldi M**, Angulo MC, Allen BD, Amin AN, Nguyen QA, Katona I, Baulch JE, Limoli CL, Soltesz I (2021) Detrimental impacts of mixed-ion radiation on nervous system function. *Neurobiol Dis* 151, 105252.

5. Lee SH, Dudok B, Parihar VK, Jung K-M, **Zöldi M**, Kang Y-J, Maroso M, Alexander AL, Nelson GA, Piomelli D, Katona I, Limoli CL, Soltesz I (2016) Neurophysiology of space travel: energetic solar particles cause cell type-specific plasticity of neurotransmission. *Brain Struct Funct* 222, 2345–2357.

6. Csincsi AI, Kopp A, **Zöldi M**, Banlaki Z, Uzonyi B, Hebecker M, Caesar JJ, Pickering MC, Daigo K, Hamakubo T, Lea SM, de Jorge GE, Józsi M (2015) Factor H-Related Protein 5 Interacts with Pentraxin 3 and the Extracellular Matrix and Modulates Complement Activation. *J Immunol* 194, 4963-4973.

10. Acknowledgements

I am truly grateful to many people for the completion of this thesis. First, I would like to thank my supervisor, István Katona, for the opportunity to work with him. He not only introduced me to neuroscience but also gave me a taste of the American lifestyle and reintroduced me to the world of birdwatching. I hope to carry forward his enthusiasm, both in science and beyond, as well as his community-building spirit. The members of our group have all been incredibly supportive in maintaining a friendly and positive atmosphere and helping me navigate the more challenging times. I owe special thanks to Barna Dudok, my first direct supervisor, who guided my first steps in STORM imaging. Zsófia László, Kata Kenesei, and László Barna provided invaluable support in bringing this project to life.

I am perhaps even more grateful for the emotional support from my family and friends than for the professional guidance. Although the constant "how's your PhD going?" questions often drove me crazy, I know their concern was essential for me to close this chapter of my life.